The Journal of Chemical Physics

RESEARCH ARTICLE | JUNE 25 2026

Modeling crossflow filtration: Effect of shear on particle-enriched polarization and cake layers

Gun Woo Park ; Jan K. G. Dhont ; Gerhard Nägele

J. Chem. Phys. 164, 244119 (2026)
https://doi.org/10.1063/5.0336005

The Journal of Chemical Physics ARTICLE pubs.aip.org/aip/jcp

Modeling crossflow filtration: Effect of shear on particle-enriched polarization and cake layers

Cite as: J. Chem. Phys. 164, 244119 (2026); doi: 10.1063/5.0336005
Submitted: 27 March 2026 • Accepted: 8 June 2026 •
Published Online: 25 June 2026

Gun Woo Park,[a] Jan K. G. Dhont, and Gerhard Nägele

AFFILIATIONS

Institute of Biological Information Processing, IBI-4, Forschungszentrum Jülich GmbH, 52425 Jülich, Germany

[a]**Current address:** Leibniz Institute for New Materials, 66123 Saarbrücken, Germany.
Author to whom correspondence should be addressed: g.park@fz-juelich.de

ABSTRACT

Crossflow filtration is a pressure-driven separation and enrichment process of colloidal particles, where a feed dispersion is continuously pumped through a hollow cylindrical membrane channel permeable to the solvent only. During the filtration process, particles are advected to and accumulate at the membrane, forming a fluid-like concentration polarization (CP) layer and a solid-like cake layer. Based on an accurate semi-analytic method developed in this paper, we determine spatially resolved flow and particle concentration profiles in the transition regime between ultrafiltration and microfiltration, where the effects of shear flow compete with Brownian particle motion. The results are presented for model dispersions of colloidal hard spheres, wherein we account for the shear-rate and concentration dependence of collective diffusion and viscosity, and for a thin, permeable filter cake. In particular, a non-monotonic shear-rate dependence of the axial flow across the CP layer is found. We show that the shear-rate dependence of particle transport properties gives insight into the origin of a long-standing apparent paradox related to the critical permeate flux characterizing the onset of cake formation.

I. INTRODUCTION

Crossflow filtration (CF) is widely used for continuous separation in industrial and biological applications, including water purification, protein enrichment, and vascular transport.[1–4] As schematically shown in Fig. 1, during the CF process, a steadily pumped dispersion flows inside a long channel whose wall consists of a membrane retentive to the dispersion particles but permeable to the solvent. As the dispersion passes through the channel, the solvent permeate flux induces particle advection toward the inner membrane wall, which is counterbalanced by particle diffusion away from the membrane. Owing to membrane selectivity, the rejected particles are concentrated near the inner membrane surface, forming a fluid-like concentration polarization (CP) layer. This layer increases the osmotic pressure by the particles, which counteracts the applied transmembrane pressure (TMP). The latter drives the permeate flux toward the membrane. Depending on operating conditions, particles can form a solidified (reversible) layer on the membrane surface, referred to as the filter cake. The cake is overlaid by the CP layer. The filter cake acts as an additional membrane for the solvent molecules, thereby increasing the hydraulic resistance of the CF setup. The details of Fig. 1 and the precise meaning of the parameters and symbols in this figure are explained in Sec. II A.

The selectivity and permeability of the membrane are important factors in the filtration process and are influenced by the pore size distribution and morphology as well as the membrane surface treatment. CF processes are commonly categorized according to the mean size of the dispersion particles. In ultrafiltration (UF) of Brownian particles, the mean particle radius is in the range from a few to about one hundred nanometers, while microfiltration (MF) refers to the filtration of large non-Brownian particles of size in the micrometer range.

Regarding Brownian particles, an increase in particle size for a given particle volume fraction strongly reduces the osmotic pressure and, consequently, its influence on the CP layer and permeate flux. Considering that the applied TMP across the membrane and cake layer often reaches 10 kPa, such as in water purification, the osmotic pressure effect of the CP layer becomes negligible for a mean particle radius exceeding 10 nm. Moreover, since collective diffusion (and self-diffusion) of Brownian particles decreases with

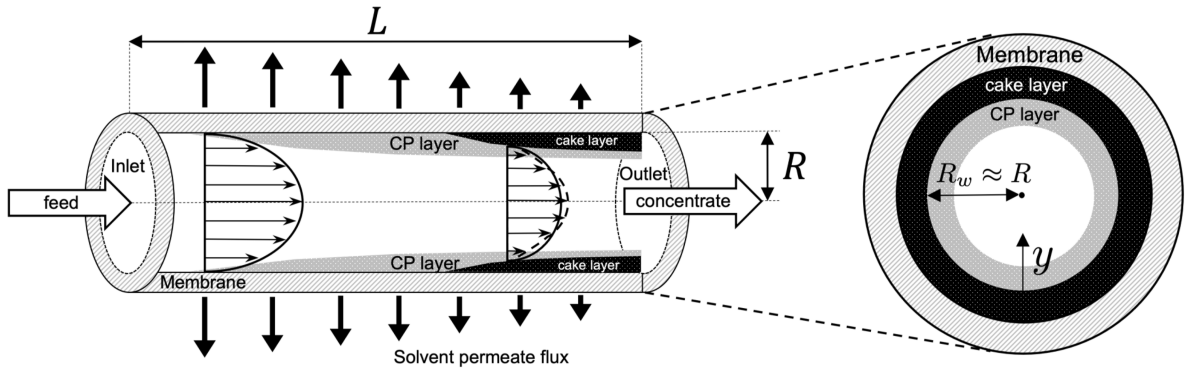

FIG. 1. Schematic view of inside–out crossflow filtration in a cylindrical membrane channel of length L and inner radius $R \ll L$. The thicknesses of the CP and cake layers are small compared to R, i.e., $R_w \approx R$, and they are exaggerated in the figure for better visibility. The axial coordinate z is taken along the channel axis, while the radial coordinate y is directed from the inner surface of the membrane or cake layer toward the channel center. The solvent permeate flux is driven by the transmembrane pressure (TMP), defined as transversal (local) pressure difference between the fluid dispersion inside the membrane channel and the outside solvent permeate.

increasing size, larger particles are more likely to form a cake layer. The minimal TMP for which a cake layer appears is referred to as *critical* TMP. The corresponding length-averaged mean permeate flux is denoted as *critical* flux, $\langle v_w \rangle_L^*$. Owing to the detrimental effects of cake formation on the CF efficiency in the form of reduced concentrate output and increased energy consumption, it is important to identify cake-forming operating conditions as quantified by $\langle v_w \rangle_L^*$.

Early CF model calculations of the critical flux were based on film theory, i.e., a one-dimensional convective-diffusion equation for the radial flow across the CP layer (film), combined with the concept of a mass-transfer (particles-transfer) coefficient,[5–8] as adopted from the Lévêque similarity solution of heat transfer problems.[9] These calculations suggest a power-law relation between critical flux and the particle radius, a, of monodisperse dispersions of Brownian particles according to $\langle v_w \rangle_L^* \propto a^{-2/3}$, while a different power law scaling $\langle v_w \rangle_L^* \propto a^{4/3}$ is predicted for large particles where shear-induced hydrodynamic diffusion is dominant and Brownian motion is negligible. When the particle radius exceeds roughly 100 nm, these models significantly underestimate the experimentally measured critical flux. The discrepancy between these model predictions and experimental data is referred to as the critical flux paradox of CF.[10–12] While various physical mechanisms have been considered subsequently, including shear-induced diffusion and migration,[8,13] inertial lift,[10] and various types of interactions between particle aggregates as well as between particles and membrane,[14,15] the flux paradox is still not fully resolved.[12] In particular, the transition regime from crossflow ultrafiltration (UF) to microfiltration (MF) for which Brownian motion is still influential, but shear-induced hydrodynamics comes into play, is still unexplored to a larger extent. For this reason, this paper focuses on the UF to MF transition regime of crossflow filtration.

Since we are also concerned with concentration and shear effects on the fluid-like CP boundary layer, we point here to earlier CF boundary layer analyses by Davis and Leighton,[16] and Romero and Davis.[17] These authors examined the axial velocity profile within the CP layer, influenced by the concentration-dependent effective dispersion viscosity. Using a simplified treatment of axial particle transport in the bulk region outside the thin CP layer, they derived semi-analytic expressions relating the particle flux in the CP layer to the operating and membrane conditions specifying the CF process. These expressions depend functionally on the particle concentration profile near the membrane surface and have been used to establish a criterion for thin cake formation similar to ours.[17] Different from their approach, we calculate flow and concentration profiles self-consistently. In addition, we account for the effect of shear in the UF to MF transition regime, including viscosity shear-thinning and shear-enhanced diffusion with Brownian motion effects included. In addition, in their case, a different threshold value of $\phi = 0.6$ is used. Their work addresses microfiltration conditions with large shear rates, where crystallization is suppressed and solidification into an amorphous cake occurs with concentrations close to the random close packing value, $\phi = 0.64$.

Davis and Sherwood[18] derived a similarity solution for the steady-state excess particle flux as a function of operating conditions, which has been widely used for modeling CF processes.[7,19] The boundary layer methods noted above oversimplify, to some extent, the flow and concentration profiles in both the CP layer and the bulk region. It has subsequently been shown that realistic flow profiles are quite complex even for pure solvent (PS) flow, i.e., for vanishing CP layer,[20–22] and for suspension flow, where, for simplicity, only first-order in concentration expressions for the osmotic pressure and radial diffusivity have been used.[23]

Recently, Park and Nägele[22,24] introduced a modified boundary layer approximation (mBLA) method for CF, in which the flow and concentration profiles are determined from general (concentration-dependent) dispersion properties. By invoking global particle flux conservation, the semi-analytic mBLA method allows for an implicit numerical calculation of the flow and particle concentration fields both in radial and axial directions. They demonstrated that the mBLA-generated fields are in distinctly better agreement with finite element (FEM) calculations than earlier similarity solution predictions. Using realistic expressions for the concentration-dependent effective viscosity and collective diffusion coefficient, the mBLA method has been applied to suspensions of hard spheres (HS), either non-permeable or permeable by the solvent, under conditions where

no cake layer forms. The semi-analytic mBLA expressions are useful for identifying general trends and unexpected features of CF, such as non-monotonic membrane wall concentration profiles. Furthermore, the method provides physical insight into the functional forms of the flow and concentration profiles, as well as global process indicators. The mBLA method has been extended to different membrane geometries, ranging from cylindrical to flat-sheet geometries with one or two flat membranes, respectively. It was shown that, irrespective of membrane geometry, among the many input and operating parameters, CF process indicators, such as the global solvent recovery indicator, are essentially determined by only three independent dimensionless variables.

The semi-analytic mBLA method has led to several important observations. First, the increased dispersion viscosity of the CP layer leads to a non-monotonic radial shear rate profile. Second, in comparison with simplifying CF calculations for hard-sphere dispersions where constant (i.e., concentration-independent) transport properties are used, the antagonistic influences of enlarged viscosity, which tends to enhance particle concentration, and enlarged radial diffusivity, which tends to lower concentration, cause a radial expansion of the CP layer with increased concentration values. Third, the earlier obtained CF similarity solution becomes strictly applicable only when the influence of permeate flux on the overall flow profile is sufficiently small.

In this paper, we extend the mBLA method to stationary inside–out CF in a cylindrical membrane setup for conditions where the dispersion microstructure is only weakly to moderately perturbed by shear flow and where a thin stationary cake layer is formed. Accordingly, the UF to MF transition regime is characterized by a single-particle characteristic shear Péclet number, Pe_a^0, of values in the range $\mathcal{O}[1-10]$, corresponding to a viscosity-rescaled Péclet number $Pe_a^f = \mathcal{O}[1]$. Only thin cake layers of mean thickness that are small compared to the inner radius, R, of the hollow cylindrical membrane are considered. In the extended mBLA method, we account for both the concentration- and shear-rate-dependent dispersion properties.

As a simple generic dispersion system, monodisperse colloidal hard spheres (HS) are used, fully characterized by their hard-core radius a and volume fraction ϕ. It is challenging to derive general expressions for the macroscopic collective dispersion diffusivity and viscosity when both Brownian motion and shear-related hydrodynamic effects are relevant, as in the UF to MF transition regime.[25–28] We use an analytic expression for the shear-affected collective diffusion coefficient of colloidal hard spheres, derived by Jin *et al.*[29] on the basis of the generalized Smoluchowski equation governing the dispersion dynamics and accompanying Brownian dynamics simulations. While Brownian motion and excluded volume particle interactions are accounted for in these simulations, solvent-mediated hydrodynamic interactions (HI) between the hard spheres are disregarded. Here, we account for HI using a hydrodynamic rescaling of the diffusion coefficient provided by Jin *et al.*,[29] using the equilibrium sedimentation coefficient where HI are fully accounted for as in Refs. 30 and 31. The rescaling procedure is similar to that used for CF by Kim and Liu.[32,33] Shear-thinning of the suspension viscosity is accounted for using an empirical Cross-type formula given in the work by de Kruif *et al.*[34] and Mewis and Wagner,[35] which we refer to as the Williams viscosity expression.

The results from the extended mBLA method are discussed for two sets of operating conditions termed C1 and C2. The first set is representative of UF setups, in which shear effects are negligible, compared to Brownian motion, yet a thin cake can form. The second set is representative of the UF to MF transition regime. Its consideration allows for unraveling the effects of shear-enhanced collective Brownian diffusion and viscosity thinning on filtration properties. These properties include flow and concentration profiles, the surface coverage of the cake layer, and the onset of cake formation as quantified by the critical flux $\langle v_w\rangle_L^*$ and associated characteristic TMP. To assess the effects of shear and local particle concentration, our generalized mBLA predictions are compared with simplifying mBLA results where viscosity shear-thinning and shear-enhancement of radial diffusion are disregarded. Progressing from the general mBLA solutions, simplified analytic expressions for flow and concentration profiles, and for the critical flux, $\langle v_w\rangle_L^*$ values are derived from assuming constant, i.e., concentration and shear-independent transport properties. If the dispersion flow is approximated by the Hagen–Poiseuille (HP) profile, earlier theoretical expressions for $\langle v_w\rangle_L^*$ in terms of the wall concentration profile are recovered, allowing for an assessment of the application range and accuracy of the latter expressions. A key finding obtained from the extended mBLA method is the shear-induced up-turn of the critical permeate flux as a function of the particle radius, for radius values exceeding 100 nm. This gives insight into the origin of the critical flux paradox.

This paper is organized as follows: Sec. II describes the employed cylindrical CF model and the underlying macroscopic transport equations. We then introduce thin cake layer modeling and demonstrate its validity via the dependence of hydrodynamic permeability on particle size and concentration. This is followed by a discussion of analytic expressions for the concentration- and shear-rate-dependent radial diffusion coefficient and the dispersion viscosity of colloidal hard spheres. The essentials of the mBLA method, with its asymptotically matched flow and concentration profiles generalized to shear-rate dependent transport properties, are given in Sec. III. Furthermore, it is described therein how a thin cake layer is accounted for. A fixed-point iteration (FPI) method used for the numerical solution of the extended mBLA equations is described in Appendix A. Section IV, in combination with Appendix B, provides a simplified analytic expression for the critical permeate flux, which allows for relating the generalized mBLA method to earlier CF model calculations. Numerical results are presented in Sec. V, first for the parameter set C1, where shear-induced effects are negligible (in Subsection V A), and subsequently (in Subsection V B), for parameter set C2 representative of the UF to MF transition regime, where shear-induced effects come into play. Our conclusions are contained in Sec. VI.

II. MODELING CROSSFLOW FILTRATION

In this section, we first formulate the basic equations governing crossflow filtration of monodisperse dispersions under steady-state conditions, where, except for a developed cake layer, no other foulants are present. Subsequently, we proceed to explain the additional approximations introduced to describe monodisperse colloidal hard-sphere dispersions under shear.

A. Basic equations

As illustrated in Fig. 1, we consider a dispersion of monodisperse colloidal spheres of radius a and feed volume fraction $\phi_b \ll 1$ at the channel inlet, steadily pumped through a cylindrical membrane channel of inner radius, R, and channel length $L \gg R$ extending along the z-direction. The membrane is assumed to be fully retentive to the spheres, but permeable to the Newtonian solvent. The velocity field of the feed dispersion at the inlet port (at axial coordinate $z = 0$) is taken to be a fully developed Hagen–Poiseuille (HP) parabolic flow in axial direction. The prescribed operating conditions are the axial velocity at the inlet-center, u^0, the dispersion pressure at the outlet port, $P^L = P(z = L)$, and the constant pressure, P^{perm}, of the solvent permeated into the solvent reservoir outside the membrane channel.

In the described inside–out crossflow filtration (CF) setup, the solvent permeates the membrane from the inner (lumen) side to the outer (permeate) side of the membrane, driven by the local transmembrane pressure difference, $\mathrm{TMP}(z) = P(z) - P^{perm}$, in the radial direction. The colloidal particles are advected toward the membrane and are accumulated at the lumen side of the membrane channel where they form a particle-enriched layer. The radial concentration profile of this fluid-like concentration polarization (CP) layer is determined by diffusive colloidal transport mechanisms directed away and flow convection directed toward the membrane. As illustrated in Fig. 1, the overall concentration and thickness of the CP layer increase with increasing axial distance z from the inlet. For a sufficiently high particle concentration, particles are immobilized and, therefore, act as an additional membrane. This so-called cake layer increases the overall hydraulic resistance of the setup and, thereby, lowers the filtration efficiency. Only reversible cake formation is considered in this work, whereas non-reversible fouling mechanisms such as membrane pores blocking and particle adsorption layers are disregarded.

Since $R \gg a$, the dispersion crossflow is described on a coarse-grained, continuum mechanics level, where individual colloidal particles and membrane pores are not spatially resolved. We consider monodisperse colloidal particles suspended in water as the solvent. To unravel the effect of the particle size on the CF process, particle radii are considered in the range of $a = 3$–200 nm. The channel Reynolds number is $Re_R \lesssim 2000$, so that the dispersion flow is described as laminar. The particle Reynolds number is $Re_a \ll 1$, such that inertial effects on particles and solvent are negligible.

This paper addresses the transition regime between ultrafiltration (UF) and microfiltration (MF), for which the characteristic particle Péclet number, $Pe_a^0 = \dot{\gamma}_w^0\, a^2/D_0$ before rescaling by the dispersion viscosity, is no larger than 120. Here, $\dot{\gamma}_w^0$ is the shear rate of the dilute feed dispersion measured at the inlet wall, and $D_0 = k_B T/(6\pi\eta_s a)$ is the Stokes–Einstein–Sutherland single-particle diffusion coefficient, where η_s is the solvent shear viscosity and $k_B T$ is the thermal energy. For non-small Pe_a^0, the dispersion is significantly perturbed away from isotropic equilibrium and its transport coefficients become shear-rate-dependent.

The axisymmetric, steady-state dispersion transport inside the channel is characterized by the dispersion-averaged, spatially varying velocity $\mathbf{V}(\mathbf{r})$, particle-volume fraction $\phi(\mathbf{r})$, dispersion pressure $P(\mathbf{r})$, dispersion viscosity $\eta(\phi, \dot{\gamma})$, and shear-enhanced radial diffusion coefficient $D_{yy}(\phi, \dot{\gamma})$. The local shear-rate, $\dot{\gamma}(\mathbf{r})$, is position-dependent in general. The vector $\mathbf{r}$ points to positions of the fluid dispersion inside the channel. For $Re_a \ll 1$, the momentum balance for the dispersion-averaged, steady-state laminar flow is described by the effective Stokes equation,

$$\nabla P = \eta \Delta \mathbf{V} + \left[\nabla \mathbf{V} + (\nabla \mathbf{V})^T\right] \cdot \nabla \eta, \tag{1}$$

in combination with the incompressibility condition,

$$0 = \nabla \cdot \mathbf{V}. \tag{2}$$

Here, $P(\mathbf{r}) = p_s(\mathbf{r}) + \Pi(\phi(\mathbf{r}), \dot{\gamma}(\mathbf{r}))$ is the sum of a solvent-phase pressure contribution, p_s, and a (generalized) shear-rate dependent osmotic pressure Π.[36] The solvent pressure part adjusts itself, such that the incompressibility constraint, $\nabla \cdot \mathbf{V} = 0$, is maintained at all positions inside the dispersion. In using the effective Stokes equation, we neglect higher-order gradients in the shear-rate[36] as well as normal-stress-difference effects.

Conservation of the number of colloidal particles (i.e., mass conservation) is quantified by the stationary continuity equation $\nabla \cdot \mathbf{J} = 0$, where the dispersion-averaged local particles' flux,

$$\mathbf{J} = \phi \mathbf{V} - \mathbf{D} \cdot \nabla \phi - \boldsymbol{\xi} \cdot \nabla \dot{\gamma} \tag{3}$$

consists of advection, Brownian plus shear-induced diffusion, and shear-induced migration parts, respectively. Here, $\mathbf{D}$ is a shear-rate-dependent long-time collective diffusion matrix. For zero shear, it reduces to the diagonal collective diffusion matrix at equilibrium, $\mathbf{D} = D_c \mathbf{I}$, where $D_c = D_0\, K_{sed}^{eq}/S^{eq}(0)$ is the long-time collective diffusion coefficient and $\mathbf{I}$ is the three-dimensional unit matrix. Moreover, K_{sed}^{eq} is the long-time sedimentation coefficient at equilibrium and $S^{eq}(0)$ is the equilibrium osmotic compressibility coefficient.[37] The third flux contribution, characterized by the shear-gradient coefficients matrix $\boldsymbol{\xi}$, describes shear-induced migration.[29] Note that $\boldsymbol{\xi} \to \mathbf{0}$ in the zero shear limit. Substitution of $\mathbf{J}$ into the stationary continuity equation gives rise to the stationary advection–diffusion equation,

$$\mathbf{V} \cdot \nabla \phi = \nabla \cdot (\mathbf{D} \cdot \nabla \phi) + \nabla \cdot (\boldsymbol{\xi} \cdot \nabla \dot{\gamma}). \tag{4}$$

Since transversal momentum diffusion in a (practically) incompressible solvent is faster than particle diffusion, a steady-state dispersion flow is established more quickly than the steady-state CP layer. The latter, in turn, is established faster than the cake layer. In this work, we analyze crossflow filtration under conditions where a complete steady state of dispersion and cake has been established.

For the considered axisymmetric flow without swirling, the flow inside the channel is described by the dispersion-averaged velocity field,

$$\mathbf{V}(y, z) = v(y, z)\, \hat{\mathbf{y}} + u(y, z)\, \hat{\mathbf{z}}, \tag{5}$$

where z measures the axial distance from the inlet and y is the radial distance from the membrane wall extending toward the central axis of the channel (see Fig. 1), with according unit vectors, $\hat{\mathbf{y}}$ and $\hat{\mathbf{z}}$, respectively. Here, v and u are the radial and axial components of the dispersion velocity, respectively. The velocity field at the inlet port is taken as fully developed parabolic HP flow in the axial direction, i.e., $v(z = 0, y) = 0$ and $u(z = 0, y) = u_{HP}(y)$ for $0 \le y \le R$, where

$$u_{HP}(y) = u^0 \left[1 - (1 - y/R)^2\right], \tag{6}$$

with $u_{HP}(y \ll R) \approx 2u^0 y/R$. Here, $u^0 = u(R,0) > 0$ is the feed dispersion velocity at the inlet center.

The zero flux boundary condition, $\mathbf{J} \cdot \hat{\mathbf{y}} = 0$, is used at the inner membrane wall. It is valid for a fully particle-retentive membrane. When a thin cake layer is formed at the inner membrane surface, the same no-flux condition is applied to the inner cake surface, where it expresses now a balance of ingoing and outgoing particles.

The boundary condition for the radial velocity component of the permeating solvent, $v_w(z) = -v(y = 0, z)$, at the inner membrane or cake surface $y = 0$, is described by the Darcy–Starling condition,

$$v_w(z) = L_P(z)\left[P(z) - P^{\text{perm}} - \Pi(\phi_w(z), \dot{\gamma}(z))\right], \tag{7}$$

where $\phi_w(z) = \phi(y = 0, z)$ is the volume fraction of particles at the inner membrane or cake surface, respectively, at distance z from the membrane inlet. Moreover, $L_P(z)$ is the cumulative hydraulic permeability at z of the membrane plus cake layer. The radial velocity, $v_w(z)$, is commonly referred to as local permeate flux, while Π is the shear-rate-dependent particle osmotic pressure.[29] As noted before, $P(z) - P^{perm}$ is the local TMP and $P(z)$ is the dispersion pressure at distance z from the channel inlet. The wall osmotic pressure, Π, operates against the local TMP and thus reduces the permeate flux. Since $\Pi \propto 1/a^3$ is valid to equilibrium, the osmotic pressure contribution to the Darcy–Starling condition is important for small particles, for which the effect of shear is small owing to $Pe_a^0 \sim a^3$. The Darcy–Starling condition is obtained from integrating the radial Darcy equation, $v = -(\kappa/\eta_s)dp_s/dy$, describing the pore-averaged radial solvent flow, v, radial pressure gradient, dp_s/dy, and Darcy permeabilities, κ, inside membrane and cake layers, respectively, across their overall radial thickness.[21,22] In addition, $p_s = P - \Pi$ is used inside the dispersion and $p_s = P^{perm}$ in the pure solvent permeate. At the inner surface of the membrane or cake layer, the no-slip axial velocity boundary condition, $u(y = 0, z) = 0$, is used since the axial solvent velocity inside membrane and cake layers is sufficiently small compared to the axial velocity inside the lumen.[21,22] On disregarding the thickness of the thin cake layer, the zero-axial flow and zero-radial flux boundary conditions are taken at $y = 0$, even when the cake is present.

B. Thin cake layer modeling

To quantify the influence of a thin reversible cake layer, we resort to a simplified description where the cake is accounted for by the hydraulic permeability, $L_P(z)$, which enters the Darcy–Starling boundary condition. The constriction of the channel in the presence of a thick cake layer is hereby disregarded. From the integrated Darcy law described above, it follows the additivity of the hydraulic resistances of the membrane plus cake layers, expressed as

$$L_P(z) = \frac{L_P^0}{1 + R_c(z)/R_P^0}, \tag{8}$$

where $R_P^0 = 1/(\eta_s L_P^0)$ is the constant hydraulic resistance of the membrane having the physical dimension of an inverse length and $R_c(z)$ is the axially varying hydraulic resistance of the cake layer. It holds $R_c(z) = 0$ for concentrations $\phi_w(z)$ below a threshold value. We identify this threshold value with the freezing transition volume fraction $\phi_f = 0.494$ where the hard-sphere dispersion solidifies for small $Pe_a^0 \ll 1$. In a z-interval, where the threshold volume fraction is reached at the membrane surface, $\phi_w(z) = \phi_f$ and $\Pi = \Pi^{eq}(\phi_f)$ are taken. As explained in the upcoming boundary layer analysis applicable to thin CP and cake layers, $\phi_w(z)$ and $R_c(z)$ are determined self-consistently from an asymptotically matched boundary layer solution, in combination with the requirement that the cross-sectionally averaged axial particle flux is z-independent. While mechanical pressure decreases across the membrane and cake layers, due to $u(y = R, z) \gg v_w(z)$ and $R/L \ll 1$ valid in UF and MF, there is practically no viscous radial pressure drop in the fluid (bulk plus CP layer) phase, i.e., $dP/dy = 0$ holds throughout the fluid phase.

While we disregard the geometric thickness of the cake layer here, as an *a posteriori* consistency check, the nominal cake layer thickness, $h_c(z)$, can be determined using Eq. (8) as

$$h_c(z) = \frac{\kappa_c}{\eta_s}\left(\frac{1}{\frac{1}{L_P(z)} - \frac{1}{L_P^0}}\right). \tag{9}$$

Here, $L_P(z)$ is the combined hydraulic permeability of membrane and cake layers, which, explained in Sec. III, is obtained from a numerical solution of underlying boundary layer analysis. Furthermore, κ_c is the Darcy solvent permeability of the cake layer taken for $\phi = \phi_f$. The permeability κ_c can be described by a variant of the empirical Kozeny–Carman relation, specialized to the Darcy permeability of a homogeneous hard-sphere cake of volume fraction ϕ. This variant is known as Ergun's equation and reads[3,38]

$$\kappa_c(a, \phi) = \frac{4}{180}\frac{(1-\phi)^3}{\phi^2}a^2. \tag{10}$$

Evaluation of Ergun's equation for the freezing transition volume fraction gives $\kappa_c(a, \phi_f) = 0.0118a^2$. According to van der Sman,[39] Stokesian dynamics simulation data for the Darcy permeability of an ordered FCC array of spheres with stick hydrodynamic boundary conditions are well approximated by Ergun's equation, but with the prefactor $4/180 \approx 0.022$ replaced by 0.020, which amounts to a 10% difference in κ_c. It is noted here that the modulus of the average hydrodynamic drag force per particle, F_d, on a homogeneous array of spheres, normalized by the Stokes drag force modulus for a single sphere, $F_{St} = 6\pi\eta_s a v$, is related to the Darcy permeability of the stationary array by $\kappa_c = 2a^2/(9\phi F)$, where $F = F_d/F_{st}$.[40] This relation for κ_c in terms of F follows from $F_d = |\langle \nabla p_s \rangle|/n$, valid under steady-state conditions, in conjunction with the modulus, $v = (\kappa_c/\eta_s)|\langle \nabla p_s \rangle|$, of the Darcy equation. Here, n is the particle number density, $\langle p_s \rangle$ is the array-averaged pressure gradient, and v is the modulus of the array-averaged flow velocity inside the bulk region of the array. Values for F as a function of ϕ are tabulated in Refs. 39–41, for different arrays of hard spheres under low-Reynolds number condition $Re_a \ll 1$.

In this work, we are particularly interested in the onset of reversible (thin) cake formation under UF conditions also, where shear effects are negligible and where a hard-sphere dispersion first solidifies at $\phi = \phi_f \approx 0.494$. This motivates our usage of the freezing transition concentration, ϕ_f, as a simplified threshold for cake formation. Note that for a thin cake layer, the internal structure of the cake layer is not significant. An accurate description of reversible

and irreversible cake formation requires an in-depth study of solidification under shear conditions, which is beyond the scope of the present paper. We restrict ourselves to a reversibly formed thin cake layer of colloidal hard spheres, which interact among themselves and with the membrane by excluded volume forces only. For the parameters used in this work, the obtained results for $R_c(z)$ and the effective cake thickness $h_c(z)$ are fully consistent with the thin cake height assumption $h_c(z) \ll R$.

C. Properties of hard-sphere dispersions

We describe here approximate expressions used for the shear- and concentration-dependence of the transport coefficients and of the generalized osmotic pressure of colloidal hard spheres entering into the basic crossflow equations discussed in Subsection II A. The shear- and concentration-dependent viscosity, $\eta(\phi, \dot{\gamma})$, in the effective Stokes Eq. (1) is approximated by the empirical Williams viscosity expression,[42]

$$\eta(\phi, \tilde{\tau}) = \eta_\infty(\phi) + \frac{\eta_0(\phi) - \eta_\infty(\phi)}{1 + |\tilde{\tau}|}, \tag{11}$$

where $\tilde{\tau} = \tau/(b\,\tau_{th})$ is the shear stress τ in units of the thermal stress $\tau_{th} = k_B T/a^3$ multiplied by the factor $b = 2.32$. The Williams expression describes shear thinning but not shear-thickening. Hydrodynamic shear-thickening occurs for colloidal hard spheres at large $Pe_a^0 \gtrsim 10$, which is not considered in this work. Equation (11) interpolates monotonically between zero-shear viscosity $\eta_0(\phi)$ and high-shear rate limiting viscosity $\eta_\infty(\phi) < \eta_0(\phi)$. The viscosity $\eta_\infty(\phi)$ is the plateau viscosity at high shear stresses prior to possibly occurring shear thickening. The latter effect, not considered here, is significant only for very strongly sheared, concentrated dispersions of hard spheres with perfectly stick hydrodynamic surface boundary conditions, where lubrication is strong and transient hydroclusters are formed.[35] The two limiting viscosities noted above are approximated by the Krieger–Dougherty type equations,

$$\eta_{\{0,\infty\}}(\phi) = \eta_s\left(1 - \frac{\phi}{\phi_{\max,\{0,\infty\}}}\right)^{-2}, \tag{12}$$

where η_s is the solvent viscosity, $\phi_{\max,0} = 0.63$ and $\phi_{\max,\infty} = 0.71$. In our subsequent boundary layer analysis of CF, it is preferable to use viscosity expressions directly in terms of the shear stress, rather than in terms of the shear rate.

The viscosity $\eta(\phi, \tilde{\tau})$ is plotted in Fig. 2 as a function of ϕ, for selected values of $\tilde{\tau}$ as indicated in the figure (left panel), and as a function of $\tilde{\tau}$ for selected values of ϕ (right panel). The above-mentioned expressions for the zero- and high-shear viscosities, and for the shear-stress dependence of the viscosity, are in good agreement with experimental data on hard-sphere dispersions.[35] This is exemplified in both figure parts in comparison with experimental data by de Kruif *et al.*[34] and Krieger,[42] respectively. It is noticed in the right panel that significant viscosity shear thinning occurs for volume fractions $\phi \gtrsim 0.3$ only.

The osmotic pressure appearing in the Darcy–Starling condition in Eq. (7) is approximated by the Carnahan–Starling equilibrium expression,

$$\Pi^{eq}(\phi) = \frac{k_B T}{V_a}\phi\frac{1 + \phi + \phi^2 - \phi^3}{(1-\phi)^3}, \tag{13}$$

with particle volume $V_a = (4/3)\pi a^3$, which for given ϕ scales like the thermal stress $k_B T/a^3$. An estimate of the relative importance of the neglected contribution, $\Pi - \Pi^{eq}$, to the generalized osmotic pressure Π of hard spheres has been provided by Jin *et al.*[29] in terms of the contact value of the isotropic part of the shear-distorted pair distribution function. According to this estimate, the relative increase in the osmotic pressure due to shear flow becomes significant only for the largest considered volume fraction and Pe_a number. Note that according to Jin *et al.*,[29] the shear correction to Π exhibits the same scaling by $k_B T/a^3$ as Π^{eq}. Due to this scaling, the influence of the osmotic pressure in the Darcy–Starling condition in Eq. (7) for $a > 10$ nm is small compared to typical crossflow TMP values.

In the advection-diffusion Eq. (4), for consistency, we disregard the shear-gradient contribution to the particle flux since this contribution arises from the shear-rate dependence of the generalized osmotic pressure, which we have similarly neglected, for reasons given above.

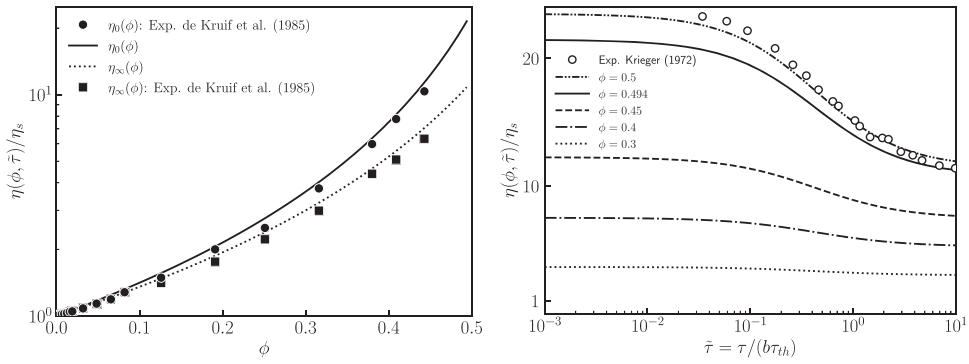

FIG. 2. Left panel: Zero-shear and high-shear rate limiting viscosities, $\eta_0(\phi)$ and $\eta_\infty(\phi)$, respectively, obtained from Eq. (12), in comparison with experimental data (filled squares and circles) for hard spheres by de Kruif *et al.*[34] Right panel: Shear viscosity, $\eta(\phi, \tilde{\tau})$, according to Eq. (11), as a function of reduced shear stress, $\tilde{\tau} = \tau/(b\tau_{th})$, for $b = 2.32$ and various ϕ as indicated. For $\phi = 0.5$, experimental viscosity data by Krieger[42] are also shown (open circles). All viscosities are non-dimensionalized by the solvent viscosity η_s.

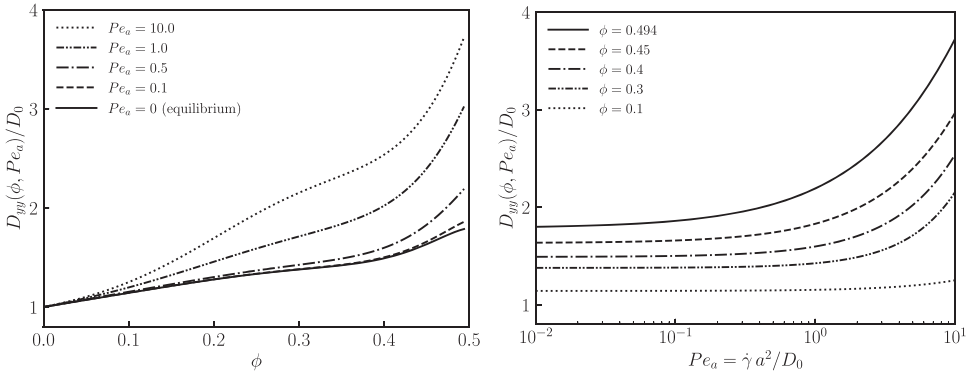

FIG. 3. Left panel: Shear-rate-dependent radial diffusion coefficient, $D_{yy}(\phi, Pe_a)$, of hard spheres determined according to Eq. (14), as a function of the volume fraction ϕ for selected Pe_a values as indicated. Right panel: $D_{yy}(\phi, Pe_a)$ as a function of Pe_a, for indicated values of ϕ. The radial diffusion coefficient is normalized by D_0.

As we argue in Sec. III, radial diffusion along the y-direction is the primary mechanism that balances particle transport near the membrane wall. Hence, only the expression for component D_{yy} in the diffusion matrix $\mathbf{D}$ is required. For this component, we use the approximated expression,[29]

$$D_{yy}(\phi, Pe_a) = D_0 K_{sed}^{eq}(\phi)\left[1 + 4\frac{\partial}{\partial\phi}\left(\phi^2 g_{iso}^{c}(\phi, Pe_a)\right)\right], \tag{14}$$

where in a crossflow setup, $\phi(y,z)$ and $Pe_a(y,z)$ are both spatially varying. Here,

$$g_{iso}^{c}(\phi, Pe_a) = \frac{1}{4\pi a^2}\oint g(\mathbf{r};\phi, Pe_a)\, dS = g_{eq}^{c}(\phi) + g_{\dot\gamma}^{c}(\phi, Pe_a) \tag{15}$$

is the orientationally averaged, shear-rate-dependent pair distribution function, $g(\mathbf{r};\ \phi, Pe_a)$, of colloidal hard spheres, which consists of an equilibrium and shear-distorted contribution, respectively. The integral extends over the surface of a central sphere. The superscript c marks contact values for two spheres at center-to-center distance $r = 2a^+$. For hard spheres in the fluid-phase state, the equilibrium contact value of the pair distribution function is given by the Carnahan–Starling expression,

$$g_{eq}^{c}(\phi) = \frac{2-\phi}{2(1-\phi)^3}. \tag{16}$$

The accordingly employed expression for $g_{\dot\gamma}^{c}$, provided by Jin *et al.*,[29] is

$$g_{\dot\gamma}^{c}(\phi, Pe_a) = C\, Pe_a^{m(\phi)}\left(1 - \frac{\phi}{\phi_{\max,0}}\right)^{-s}, \tag{17}$$

where $\phi_{\max,0} = 0.63$ is the volume fraction close to the random closed packing value of hard spheres. The dimensionless parameters in the above-mentioned equation have been obtained from Brownian dynamics simulation (without hydrodynamic interactions) as $m(\phi) = 0.43 + 5.26\phi - 8.80\phi^2$, $s = 2.525$, and $C = 0.0140$.[29]

To account overall for hydrodynamic interactions (HI) between particles disregarded by Jin *et al.*,[29] the dimensionless function,

$$K_{sed}^{eq}(\phi) = 1 - 6.5464\ \phi\left[1 - 3.348\phi + 7.426\phi^2 - 10.034\phi^3 + 5.882\phi^4\right] \tag{18}$$

is included as a factor in Eq. (14). It is a numerically accurate parameterization of the equilibrium (short-time) sedimentation coefficient of monodisperse hard spheres, as it is shown in the work of Roa *et al.*[43] An account of the effect of HI on a long-time transport property of colloidal hard spheres, made by multiplication of the long-time property without HI by the corresponding short-time property with HI, has been shown to be a good overall approximation.[44]

The volume fraction and shear-rate dependence of $D_{yy}(\phi, Pe_a)$ according to Eq. (14) is depicted in Fig. 3. As seen in the left panel, the monotonic increase in D_{yy} with increasing ϕ is significantly enhanced for larger Pe_a values. The accompanying increase in D_{yy} with increasing Pe_a, for constant ϕ, is shown in the right panel. For $Pe_a < 0.1$, the radial diffusion coefficient is close to its zero-shear value where Brownian diffusion dominates, even for the largest considered volume fraction ϕ_f where freezing sets in.

We emphasize that $D_{yy}(\phi, Pe_a)$ includes the factor $D_0 = k_B T/(6\pi\eta_s a)$. Hence, it is appropriately referred to as shear-enhanced (collective) Brownian diffusion coefficient to clearly distinguish it from the athermal, shear-induced hydrodynamic diffusion coefficient, $D_{yy}^{hyd} \propto \dot\gamma\, a^2$, characterizing the diffusion-like dynamics of large, micrometer-sized particles (suspended in water), where the influence of Brownian motion is negligible. The latter coefficient D_{yy}^{hyd} is due to many-particle hydrodynamic interactions under strong shear flow conditions where $Pe_a \gg 1$. It diminishes for small concentrations and small particle sizes.

III. MODIFIED BOUNDARY LAYER ANALYSIS OF CROSSFLOW FILTRATION

In this section, we generalize the modified boundary layer analysis (mBLA) method, introduced for UF by Park and Nägele,[22] to non-small Pe_a^0 where shear effects matter and to conditions where a thin cake layer is formed. Since details of the mBLA method have been presented earlier,[22] we focus here on its extension to shear-rate-dependent transport properties and cake layer formation.

For common operating conditions where the radial dispersion velocity v toward the membrane is small in magnitude compared to the in-flow characteristic axial velocity u^0, the CP layer is thin with characteristic thickness $\delta_{CP}^0 \ll R$. Across the CP layer, ϕ steeply decreases radially from its maximal value, $\phi(y=0,z) = \phi_w(z)$, at the membrane surface toward its minimal bulk value $\phi(y=R,z) = \phi_b$. As explained by Park and Nägele,[22] using the

smallness parameter $\varepsilon = \delta^0_{CP}/R \ll 1$ in a dominant balance analysis of the advection–diffusion equation describing the balance of diffusive radial flux away and the advective radial flux toward the membrane, this equation is singularly perturbed. Furthermore, the analysis revealed that ε can be expressed as

$$\varepsilon = \frac{1}{Pe_R} \ll 1, \tag{19}$$

where $Pe_R = Rv^0_w/D_0$ is the ratio of the diffusion time of particles, R^2/D_0, and radial flow advection time, R/v^0_w, along the channel radius R. Here, v^0_w is a characteristic value for the permeate velocity given by

$$v^0_w \equiv L^0_P \ \mathrm{TMP}^0 = L^0_P\left[\frac{2\eta_s L}{R^2}u^0 + P^L - P^{perm}\right], \tag{20}$$

where $u^0 = R^2\ \Delta P/(4\eta_s L)$, with $\Delta P = P(0) - P^L$, is the center velocity of the HP pipe flow. For later use, we have introduced here the characteristic transmembrane pressure difference TMP^0, which depends on the input operation parameters, u^0, P^L, and P^{perm}, on L and R, specifying the membrane dimensions and the solvent viscosity η_s. For a significantly developed CP layer, $Pe_R \gg 1$. In the following, we describe how the flow and concentration fields of the dispersion in the bulk region, and inside the thin CP layer region, are determined and asymptotically matched and how the thin cake layer model introduced in Sec. II B is implemented. Regarding the dispersion pressure P and radial velocity component v, no distinction is required between their respective forms in the outer bulk and inner CP boundary layer regions since to first order in ε, and different from ϕ and u, these quantities do not vary steeply across the CP layer.

A. Outer solution

The differential equations governing the flow and concentration fields in the bulk region are obtained by expanding the effective Stokes, continuity, and advection–diffusion Eqs. (1)–(4) up to zeroth order in ε. The axial and radial components of the Stokes equation in the outer region are, respectively,

$$\frac{\partial P}{\partial y} = 0, \tag{21}$$

$$\frac{\partial P}{\partial z} - \frac{\partial}{\partial y}\left(\eta(\phi,\tilde{\tau})\frac{\partial u}{\partial y}\right) = -\frac{\eta(\phi,\tilde{\tau})}{R-y}\frac{\partial u}{\partial y}, \tag{22}$$

where the non-vanishing term on the right-hand side of the second equation is due to the cylindrical curvature of the membrane. As noted earlier, there is no radial variation of the dispersion pressure $P(z)$ from the bulk region to the inner membrane or cake surfaces. The continuity equation in the outer region reads

$$\frac{\partial v}{\partial y} + \frac{\partial u}{\partial z} = \frac{v}{R-y}, \tag{23}$$

and the outer region form of the advection–diffusion equation is

$$v\frac{\partial \phi}{\partial y} + u\frac{\partial \phi}{\partial z} = 0. \tag{24}$$

Note that $D_{yy}(\phi, Pe_a) \approx D_0$ in the bulk region, where $\phi(y,z) \approx \phi_b \ll 1$.

The concentration profile in the outer bulk regime follows readily from the advection–diffusion equation as $\phi(y,z) = \phi_b$, under the proviso that ϕ_b is at most of $\mathcal{O}[\varepsilon]$. From the Stokes and continuity Eqs. (21)–(23) in the outer region, combined with a separation of variable ansatz for the y and z dependencies of the velocities, the following factorized flow solution for the axial velocity in the outer region is obtained:

$$u(y,z) = -\frac{R^2}{4\eta_s}\frac{dP}{dz}\left[1 - \left(1 - \frac{y}{R}\right)^2\right]. \tag{25}$$

In this velocity profile, the z-dependence is determined solely by the axial pressure drop from the inlet toward the outlet of the channel at $z = L$. The radial velocity in the outer region is

$$v(y,z) = -v_w(z)\left(1 - \frac{y}{R}\right)\left[2 - \left(1 - \frac{y}{R}\right)^2\right]. \tag{26}$$

Note that v is not singularly perturbed, so that the present outer region expression is also valid inside the CP layer, where $y/R \ll 1$. Recall that $v_w(z) = -v(y=0,z)$, i.e., the permeate velocity, $v_w(z)$, is taken positive for the solvent flowing inside–out from the lumen to the permeate side.

Different from our earlier studies where cake formation was disregarded, the pressure field $P(z)$ is determined as the numerical solution of

$$\left[L^0_P L^2\frac{d^2}{dz^2} - k^2 L_P(z)\right]P(z) = -k^2 L_P(z)\Pi^{eq}(\phi_w(z)), \tag{27}$$

which depends functionally on the concentration profile, $\phi_w(z)$, at the membrane or cake surface. In the presence of the cake, the non-constant cumulative hydraulic permeability, $L_P(z)$, renders the above-mentioned differential equation nonlinear. The dimensionless parameter k, with

$$k^2 = 16\left(\frac{L}{R}\right)^2\frac{\eta_s L^0_P}{R} \tag{28}$$

quantifies the effect of overall solvent permeability on the pressure profile. Larger k values give rise to a strongly non-linear axial pressure profile different from the HP profile due to a more distinct permeate flux. For the operating conditions considered in this work, $k \lesssim 0.1$.

The parameter k is related to the characteristic value, $\beta^0 = 4Lv^0_w/(Ru^0)$ of the so-called solvent recovery indicator β. This indicator is defined as the ratio of the permeate volume flow rate through the cylindrical membrane surface to the cross-sectionally averaged volume flow rate of the dispersion at the channel inlet, which is of HP form. Explicitly, β is given by

$$\beta = \frac{2\pi R\int_0^L dz\ v_w(z)}{\pi R^2 u^0/2}, \tag{29}$$

and its characteristic value β^0 follows from approximating the permeate radial velocity profile $v_w(z)$ by the characteristic value v^0_w.

B. Inner solution

Having described the solutions for the velocity, pressure, and concentration profiles in the outer region, we next discuss the inner CP boundary layer solutions whose derivation without shear-rate dependence and cake formation has been given by Park and Nägele.[22] To the zeroth order in ε, the advection–diffusion equation for the concentration profile $\phi(y,z)$ reduces inside the CP layer to

$$v\frac{\partial\phi}{\partial y} = \frac{\partial}{\partial y}\left(D_{yy}(\phi, Pe_a)\frac{\partial\phi}{\partial y}\right), \tag{30}$$

describing the balance of radial advection and diffusion currents. As discussed before, shear-induced migration is neglected, which otherwise would contribute an additional term to the advection–diffusion equation. Notice that

$$Pe_a(y,z) = \frac{a^2}{D_0}\frac{\partial u(y,z)}{\partial y} \tag{31}$$

is the dimensionless local shear rate field, to zeroth order in ε. In our dominant balance analysis, in addition to $\varepsilon \ll 1$, it is assumed that $\beta^0/4 \gg \varepsilon^2$, expressing the condition of significant solvent permeation of the membrane and cake layers.

The effective Stokes equation reduces in the CP layer region to

$$\frac{\partial}{\partial y}\left(\eta(\phi,\tilde{\tau})\frac{\partial u}{\partial y}\right) = 0, \tag{32}$$

with $\tilde{\tau} = \tau/(b\tau_{th})$, where $\tau(z) = \eta(\phi,\tilde{\tau})\partial u/\partial y$ is the local shear stress. Notice that the local shear stress is self-referenced here. The above-mentioned equation expresses that the CP layer shear stress is constant in the radial direction.

To zeroth order in ε, the continuity equation reads

$$\frac{\partial v}{\partial y} = 0, \tag{33}$$

expressing that inside the CP layer, the radial velocity is independent of y, i.e., $v(y,z) = -v_w(z)$. In combination with the zero radial particle flux at $y = 0$, and the extended Darcy–Starling and zero tangential velocity wall boundary conditions, the formal solutions for the concentration and velocity fields of the CP layer are obtained as

$$\phi(y,z) = \phi_w(z)\exp\left[-Pe_R\frac{v_w(z)}{v_w^0}\frac{1}{R}\int_0^y \frac{D_0}{D_{yy}(\phi(y',z), Pe_a(y',z))}dy'\right], \tag{34}$$

$$u(y,z) = \tau(z)\int_0^y \frac{1}{\eta(\phi(y',z),\tilde{\tau}(y',z))}dy', \tag{35}$$

$$v(y,z) = -v_w(z), \tag{36}$$

where $v_w^0 = L_P^0\ \mathrm{TMP}^0$ is the characteristic value of the permeate flux. Note that the inter-related fields, ϕ, u, v, and P, are dependent on the wall profiles, $\phi_w(z)$ and $R_c(z)$. The latter profiles enter into the CP layer description via the surface (wall) boundary conditions.

C. Asymptotic matching, particles conservation, and model consistency

To this point, the inner and outer solutions of the concentration and flow profiles are expressed as functionals of the concentration and cake hydraulic resistance wall profiles, $\phi_w(z)$ and $R_c(z)$, respectively. In an ensuing step, the outer limits of the inner solutions are asymptotically matched to the inner limits of the outer solutions, using an additive matching rule for $\phi(y,z)$ and a multiplicative matching rule for $u(y,z)$.[45] This results in the matched asymptotic solutions,

$$\phi(y,z) = (\phi_w(z) - \phi_b)\exp\left(-Pe_R\frac{v_w(z)}{v_w^0}\mathscr{I}_D(y,z)\right) + \phi_b\left(1 - Pe_R\frac{v_w(z)}{v_w^0}\mathscr{I}_D(y,z)\exp\left(-Pe_R\frac{v_w(z)}{v_w^0}\mathscr{I}_D(y,z)\right)\right), \tag{37}$$

$$u(y,z) = -\frac{R^2}{4\eta_s}\frac{dP}{dz}\left(2 - \frac{y}{R}\right)\mathscr{I}_\eta(y,z), \tag{38}$$

where the integrals,

$$\mathscr{I}_D(y,z) = \frac{1}{R}\int_0^y \frac{D_0}{D_{yy}(\phi(y',z), Pe_a(y',z))}dy', \tag{39}$$

$$\mathscr{I}_\eta(y,z) = \int_0^y \frac{\eta_s}{\eta(\phi(y',z),\tilde{\tau}(y,z))}dy'\left[\int_0^R \frac{\eta_s}{\eta(\phi(y',z),\tilde{\tau}(y,z))}dy'\right]^{-1}, \tag{40}$$

invoking the radial diffusion coefficient D_{yy} and shear viscosity η have been introduced. The denominator in $\mathscr{I}_\eta$ guarantees that the inner solution for $u(y,z)$ matches the outer solution at the channel centerline.

The pressure $P(z)$ and radial flow $v(y,z)$ require no asymptotic matching and are thus given by their respective outer solutions. For $Pe_a^0 \to 0$, D_{yy} and η become shear-rate independent, and without cake formation, the asymptotically matched solutions presented here reduce to the expressions for cylindrical geometry given by Park and Nägele.[24]

The matched asymptotic solutions are functionally dependent on the wall profiles $\phi_w(z)$ and $R_c(z)$, which, in turn, are interrelated by the extended Darcy–Starling wall boundary condition. To determine these profiles, as a global requirement, we employ conservation of the cross-sectionally integrated axial particle flux, i.e.,

$$2\pi\int_0^R dy\ (R-y)\phi(y,z)\ u(y,z) = \frac{\pi R^2}{2}\phi_b\ u^0. \tag{41}$$

This relation expresses that under steady-state conditions, and for an ideally particle-retentive membrane, the cross-sectionally integrated axial particle flux, $J_z = \mathbf{J}\cdot\hat{\mathbf{z}}$, is constant and equal to its value at the inlet. The term on the right-hand side is the inlet value of the integrated flux, obtained using $\phi(y, z=0) = \phi_b$ and the Hagen–Poiseuille form, $u_{HP}(y)$, for the inlet flow $u(y, z=0)$, where u^0 is the flow velocity at the inlet center position $(y,z) = (R,0)$. A small axial diffusion flux contribution of $\mathscr{O}[\varepsilon^2]$ is disregarded here for consistency, so that $J_z = \phi\, u$.

In the numerical analysis of our CF model for thin CP and cake layers, we combine cross-sectional particle flux conservation with the asymptotically matched (formal) flow and concentration fields solutions to calculate $\phi_w(z)$ and $R_c(z)$ iteratively. For this purpose, we use a fixed-point iteration method similar to the one employed earlier by Park and Nägele.[22] In this iteration scheme where $\phi_w(z)$ and $R_c(z)$ are determined simultaneously, one needs to distinguish z positions where the condition $\phi_w(z) = \phi_f$ of cake formation is met, from those axial positions where $\phi_w(z) < \phi_f$ and the CP layer is present only.

According to the Darcy equation introduced in Sec. II B, the height profile, $h_c(z)$, of a uniform cylindrical cake is related to its hydraulic resistance profile, $R_c(z)$, by

$$\frac{h_c(z)}{R} = \exp\{\kappa_c\, R_c(z)/R\} - 1. \tag{42}$$

For a thin cake layer, $h_c(z)$ grows linearly with the cake resistance according to $h_c(z) = \kappa_c R_c(z)$. This relation was used in obtaining Eq. (9).

Provided $h_c(z) \ll R$ holds for the employed input parameters, the mBLA method can be used. Furthermore, one readily checks for the smallness, $\delta^0_{CP} \ll R$, of the diffuse CP layer, additionally required for the validity of the mBLA method, by using $\delta^0_{CP} = D_0/v^0_w = R\,\varepsilon$ for the characteristic CP layer thickness.

This completes our discussion of the mBLA CF method, generalized here to account for the shear-rate dependence of particle transport in the UF to MF transition regime and for thin cake layer formation. Details about the iterative numerical solution of the generalized mBLA equations are presented in Appendix A.

IV. SIMPLIFIED CRITICAL FLUX CALCULATION

The particle radii of the suspensions encountered in this paper are in the range of a = 3–200 nm, with the corresponding Pe^0_a numbers limited to $Pe^0_a \lesssim 10$ for a Newtonian solvent. For the considered operating conditions, hydrodynamic effects of shear, i.e., viscosity thinning and shear-enhanced diffusion begin to compete with Brownian motion. As discussed in detail in Subsection V A, since $Pe^0_a \propto a^3$, $D_0 \propto 1/a$, and $\Pi \propto 1/a^3$, enlarging a decreases the radial diffusivity and viscosity while the osmotic pressure becomes negligible. The overall effect is to increase the particle concentration inside the CP layer, which also affects cake formation.

The minimal characteristic TMP^0 value where a cake starts to be formed in CF is denoted as the *critical* TMP value, TMP*, marked by an asterisk. The according (length-averaged) critical mean permeate flux is referred to as the *critical* flux, $\langle v_w\rangle^*$. Here, $\langle(\cdots)\rangle_L = (1/L)\int_0^L dz\,(\cdots)$ denotes an average over the length of the membrane channel. Based on the extended mBLA method, in Eq. (B11) of Appendix B, we have derived an expression for mean permeate flux in terms of the membrane and operating parameters. This general expression allows making contact with earlier results for the critical flux based on two-dimensional similarity flow solutions[18] and one-dimensional classical film theory in conjunction with the concept of a mass (i.e., particles) transfer coefficient.[5,7]

Equation (B11) invokes the radial and axial characteristic Péclet numbers, Pe_R and Pe_L, respectively. If these are replaced by their explicit forms, we obtain the general mBLA result for the mean permeate flux,

$$\langle v_w\rangle_L = \left[\frac{\dot\gamma^0_w D_0^2}{L}\frac{\phi_w(z)}{\phi_b}\frac{\Psi(z)}{G(z)}\right]^{1/3}. \tag{43}$$

This result remains valid in the presence of a thin cake and for characteristic Péclet numbers $Pe^0_a = \mathcal{O}[1-10]$, where shear effects matter. Here, $\Psi(z)$ and $G(z)$ are dimensionless functions defined in Eqs. (B9) and (B12) of Appendix B, respectively, and $\dot\gamma^0_w = 2u^0/R$ is the characteristic shear rate at the inlet membrane wall. By consistency, the right-hand side should be z-independent for $z \gg \delta^0_{CP}$, the validity of which we have cross-checked using the mBLA solutions for $\Psi(z)$ and $G(z)$. Hence, it can be taken at $z = L$. As discussed in Appendix B, $\Psi(z) \approx 1$ holds for constant transport properties and negligible osmotic pressure. In contrast, values $\Psi(z) < 1$ are expected when the particle transport inside the CP layer is slowed down by enlarged viscosity and reduced radial diffusion, whereas in the opposite case, $\Psi(z)$ can be larger than one. The function $G(z)$ accounts for the influence of $v_w(z)$ on the axial particle transport.

Equation (43) can be cast into the suggestive form

$$\langle v_w\rangle_L = K_m\left(\frac{\phi_w(L)}{\phi_b}\right)^{1/3}, \tag{44}$$

where K_m is the mass (particles) transfer coefficient given by

$$K_m = \left(\frac{\dot\gamma^0_w D_0^2}{L}\frac{\Psi(L)}{G(L)}\right)^{1/3}, \tag{45}$$

with

$$\Psi(L) = \frac{Pe_R^2(v_w(L)/v^0_w)^2}{2}\,\frac{1}{R}\int_0^R dy\,(1-y/R)(2-y/R) \times \mathscr{I}_\eta(y,L)\exp\left(-Pe_R(v_w(L)/v^0_w)\,\mathscr{I}_D(y,L)\right), \tag{46}$$

$$G(L) = \frac{u^0}{u(y=R,z=L)}\left(\frac{v_w(L)}{\langle v_w\rangle_L}\right)^2. \tag{47}$$

Notice that K_m in Eq. (45) is of a more general form than the conventional expression for the CF mass transport coefficient K^0_m based on the Lévêque solution for related heat-transfer problems.[6,8,9] According to Trettin and Doshi,[7] the latter expression valid for $\phi_w \gg \phi_b$ reads

$$K^0_m = A\left(\frac{\dot\gamma^0_w\, D_0^2}{L}\right)^{1/3}, \tag{48}$$

where $A = (3/2)^{2/3} \approx 1.31$, provided that ϕ_w is taken as constant. In fact, the mBLA expression for K_m reduces to K^0_m when simplifying assumptions are made. First, for transport properties that are assumed to be constant, $D_{yy} = D_0$ and $\eta = \eta_s$, and negligible osmotic pressure, $\Psi(z) = 1$ holds, as discussed above. Second, when the Hagen–Poiseuille profile is assumed to describe the suspension flow field $\mathbf{v}$, fully disregarding the permeate flux, $G(z)$ simplifies to

$$G^{(HP)}(z) = \left(\frac{2\left(P^L - P^{perm}\right)/\Delta P}{1 + 2\left(P^L - P^{perm}\right)/\Delta P} \right)^2, \tag{49}$$

where $\Delta P = P(0) - P^L$ is the axial pressure drop along the membrane channel. Provided the TMP at the outlet, $P^L - P^{perm}$, happens to exactly match the axial pressure drop, it follows that $G^{(HP)}(L) = (2/3)^2$, and hence, $A = (G^{(HP)}(L))^{-1/3} = (3/2)^{2/3}$ is recovered. In CF, however, one commonly has $P(0) - P^L \ll \mathrm{TMP}^0$, such that $G^{(HP)}(L) = 1$, suggesting that $A \approx 1$ should be preferentially used instead of $A = 1.31$. Note that usage of the HP flow profile is a stronger approximation than using the pure solvent flow profile, as in Eq. (B12) of Appendix B.

Next, to obtain an expression for the critical flux $\langle v_w \rangle_L^*$ characterizing the onset of cake formation, we employ the assumption that $\phi_w(z)$ is monotonically increasing in z. Although monotonicity of $\phi_w(z)$ is not always valid (see Refs. 13, 22, and 46 for counter-examples), it is often assumed in CF modeling.[47,48] For monotonic $\phi_w(z)$, cake formation appears first at the outlet, which happens when $\phi_w(L) = \phi_f$ and $\phi_w(z < L) < \phi_f$. The critical flux expression is thus

$$\langle v_w \rangle_L^* = K_m^* \left(\frac{\phi_f}{\phi_b} \right)^{1/3}, \tag{50}$$

where K_m^* is the mass transfer coefficient in Eq. (45), under critical TMP^0 conditions and for monotonic $\phi_w(z)$. The $(\phi_f/\phi_b)^{1/3}$ dependence originates from cross-sectional (axial) particle flux conservation. As recently remarked by Song,[49] this is the correct concentration dependence, rather than a logarithmic dependence predicted by film theory. The evaluation of $\langle v_w \rangle_L^*$ requires the solution of the mBLA equations, e.g., by a fixed-point iteration scheme explained in Appendix A. When shear is negligible, however, as a decent approximation, one can assume a hyperbolically shaped axial pressure drop as for pure solvent flow, in which case $G(L)$ can be calculated analytically. Moreover, $\Psi(L)$ is obtained from a numerical integration using the pure-solvent form of $v_w(L)$. Numerical results for $\langle v_w \rangle_L^*$ using this approximation are presented in Sec. V.

For small (local) Péclet numbers where viscosity thinning and shear-enhancement of radial diffusion are negligible, $\Psi(L)/G(L)$ becomes independent of a. Since $D_0 \propto 1/a$, it follows then from Eq. (45) that $K_m \propto a^{-2/3}$ and hence $\langle v_w \rangle_L \propto a^{-2/3}$, an UF result reported earlier on. For non-small Péclet numbers where the influence of shear on η and D_{yy} becomes significant, the full numerical solution of the generalized mBLA equations is required to obtain $\Psi(L)$ entering Eq. (45) for K_m. As shown in Sec. V, deviations from the $a^{-2/3}$ scaling behavior are then observed in the UF to MF transition regime of medium-sized particles of radius $a \gtrsim 100$ nm.

For large hard spheres under MF conditions of large Péclet numbers where Brownian motion is negligible compared to shear-induced hydrodynamic diffusion and migration, expressions of the form $D_{yy}^{hyd} = \dot{\gamma}\, a^2 f(\phi)$ have been commonly used for the shear-induced hydrodynamic diffusion coefficient D_{yy}^{hyd}. Here, $\dot{\gamma}$ is the (local) shear rate, and $f(\phi)$ with $f(0) = 0$ is typically a monotonically increasing function in ϕ.[50] From substituting D_0 by D_{yy}^{hyd} in the simplified mass transfer coefficient K_m^0 in Eq. (48), the scaling relation $\langle v_w \rangle_L^* \propto a^{4/3}$ follows, where the exponent 4/3 qualitatively differs from the exponent −2/3 encountered for (low-shear) Brownian diffusion.

V. RESULTS AND DISCUSSION

Using the semi-analytic mBLA method, extended to include shear flow and cake formation, we analyze the effects of shear-dependent collective diffusion and viscosity thinning on the CP layer and cake formation in inside–out crossflow filtration. As a reference dispersion, we employ monodisperse colloidal hard spheres in water at room temperature. As explained before, the membrane is modeled as a long, hollow cylindrical channel of inner radius R and length L, with $R/L \ll 1$. The membrane is assumed to be ideally particle-retentive. Except for a reversibly formed thin filter cake, no additional (irreversible) membrane fouling mechanisms, such as membrane surface adsorption of and pore blocking by particles, are considered. The extended mBLA method is used, in particular, to predict the tube-length-averaged critical permeate flux, $\langle v_w \rangle_L^*$, at which cake formation sets in.

To unravel the influence of shear, in Subsection V A, we first discuss crossflow ultrafiltration (UF) results for which $Pe_a^0 \ll 1$, such that Brownian motion is dominant, and D_{yy} and η take their zero-shear equilibrium values. The excellent accuracy of the mBLA method in the UF regime is demonstrated for axial and radial CP layer concentration profiles by comparison with finite element (FEM) calculations. Furthermore, we study the effect of a thin cake layer on the mean permeate flux $\langle v_w \rangle_L$ and determine the mean critical flux, $\langle v_w \rangle_L^*$, when a cake layer is about to be formed. Subsequently, in Subsection V B, crossflow conditions typical of the UF to MF transition regime are considered, where the influence of shear is significant. The extended mBLA method is used here to analyze concentration, axial flow, effective diffusion, and viscosity profiles characterizing the CP layer in the transition regime and to determine the critical mean permeate flux.

We first specify the employed operating parameters, namely, the axial velocity at the inlet-center, u^0, the pressure at the outlet, $P^L = 1$ atm, set equal to the atmospheric pressure, and the characteristic transmembrane pressure difference, TMP^0, defined in Eq. (20). These input parameters are complemented by selected values of parameters characterizing the membrane and dispersion. The membrane parameters are the inner radius R and length L of the hollow membrane channel, and the hydraulic permeability L_P^0 of the clean membrane, which, in combination with the operating parameters, determine the permeate pressure, P^{perm}, according to Eq. (20). The hard-sphere dispersion is characterized by the solvent viscosity, η_s, feed volume fraction $\phi_b \ll 1$ at the inlet and particle radius a. The radius a affects the single-particle Brownian diffusion coefficient, $D_0 = k_B T/(6\pi\eta_s a)$, and the characteristic Péclet number, Pe_a^0, at the inlet wall. The latter is given by $Pe_a^0 = (2\, u^0/R)a^2/D_0 \propto a^3$, where $\dot{\gamma}_w^0 = 2\, u^0/R$ is the shear rate of the incoming Hagen–Poiseuille flow at $z = 0$ and $y = 0$. The solvent viscosity, $\eta_s = 10^{-3}$ Pa s, and the diffusion coefficient, D_0, are taken for water as a solvent at room temperature $T = 293.15$ K. Particle radius values in the range $a = 3.13$–200 nm are considered, and two values $\phi_b = \{1 \times 10^{-5}, 1 \times 10^{-3}\}$ are selected for the feed concentration. For the concentration and shear-rate-dependent dispersion viscosity, η, radial diffusion coefficient D_{yy}, and osmotic pressure Π entering the mBLA method, the expressions in Eqs. (11), (13), and (14) are used,

TABLE I. Parameter sets used in this work. Set C1 is characteristic of crossflow UF, while set C2 is typical for the transition regime between crossflow UF and MF.

	L_P^0 [m/(Pa s)]	R (mm)	L (mm)	ϕ_b	u^0 (m/s)
C1	6.7×10^{-10}	0.5	500	1×10^{-3}	1.625×10^{-2}
C2	1×10^{-8}	0.5	50	1×10^{-5}	0.2

respectively. Most of the results for the mean permeate flux are calculated as functions of TMP^0, for fixed u^0 and P^L, and an accordingly adjusted P^{perm} value.

As noted in Table I, the parameters of set C1 are characteristic for dispersions of smaller particles ($a \leq 100$ nm) under UF conditions, where shear effects are negligible. The hydraulic permeability of the clean membrane in set C1 is $L_P^0 = 6.7 \times 10^{-10}$ m/(Pa s), which is a permeability value in the range of UF membranes.[3] The parameters of set C1 are similar to those used by Roa, Zholkovskiy, and Nägele[19] and by Park and Nägele,[22] where crossflow UF is considered. In contrast, the parameters of set C2 listed in Table I are typical of the UF to MF transition regime, characterized by small to moderately large Péclet numbers $Pe_a \lesssim 10$. The considered particle radii are restricted here to $a \leq 200$ nm. The hydraulic permeability $L_P^0 = 1 \times 10^{-8}$ m/(Pa s) of set C2 is about two orders of magnitude larger than that of C1, which, for equal membrane thickness, amounts to a far larger mean pore size. The parameter values of C2 are motivated by an experimental CF study by Kwon *et al.*[51] In the latter study, however, much larger particles typical for the MF regime have been considered, with very large particle Péclet numbers for which shear-induced particle migration matters but Brownian motion effects are negligible.

The parameters of sets C1 and C2 are in the validity range of the mBLA method, which requires that $R/L \ll 1$, $Re_R R/L \ll 1$, $\beta^0 \geq \mathcal{O}[\varepsilon]$, and $\phi_b \ll 1$. Furthermore, the value of the dimensionless parameter k^2 introduced in Eq. (28) is small for both sets, equal to 1×10^{-2} for C1 and 3.2×10^{-3} for C2. Small values of k^2 are common in crossflow filtration processes, with the implication that axial variations of the dispersion velocity are hardly affected by the permeate flux through the membrane and cake. Hence, the difference between the length-averaged actual TMP and the characteristic TMP^0 value introduced in Eq. (20) is negligible. According to the criteria provided by Park and Nägele,[22] the parameters of C1 and C2 are such that there is no undesired axial flow exhaustion or permeate flow reversal in the CF process.

While, for the mBLA analysis described in Sec. III, the respective thicknesses of the membrane and cake layers are not needed as input, the following self-consistency analysis allows assessing the validity of the employed thin-cake approximation. On assuming the membrane thickness, h_m, to be 20% of R, the Darcy permeability of the clean membrane is estimated, using $\kappa_m = L_P^0 \eta_s h_m$, as 235 nm^2 for set C1. Moreover, since $\kappa_c = 0.0118a^2$ according to Ergun's equation in Eq. (10), the reduced characteristic cake thickness δ_c^0/R follows, using $\delta_c^0/R = (\kappa_c/\kappa_m)(h_m/R)$, as 2.4×10^{-5}, 2.4×10^{-4}, and 0.024, for particle radius $a = 3.13$, 10, and 100 nm, respectively. For set C2 parameters, the membrane Darcy permeability is $\kappa_m \approx 10^3$ nm^2, resulting in $\delta_c^0/R = 0.023$ for the largest considered radius of $a = 200$ nm. Thus, the thin cake layer assumption is valid for both parameter sets. One similarly finds for both sets that $\delta_{CP}^0/R \ll 1$ holds for the characteristic CP layer thickness, which justifies the usage of our boundary layer analysis.

A. Crossflow ultrafiltration

Next, we discuss our results for the set C1 parameters typical of UF, where $Pe_a^0 \ll 1$, so that shear flow effects on particle transport, microstructure, and thermodynamics are negligible. The results are presented for the concentration profiles and mean permeate flux calculated for different particle sizes and characteristic TMP values. Furthermore, the influence of a thin cake layer on the mean permeate flux and the hydraulic resistance profile is investigated.

Figure 4 depicts the volume fraction profile $\phi(y = 0, z)$ in axial direction (left), and in radial direction (right) at the outlet, $\phi(y, z = L)$, respectively, for UF set C1, with $a = 10$ nm and TMP^0 values listed in the right panel. The curves denote mBLA results. Cake formation is predicted only for the largest considered $\mathrm{TMP}^0 = 10$ kPa (solid lines). The excellent accuracy of the mBLA results is illustrated for TMP values without cake formation only for comparison with results of the corresponding finite-element method (FEM) generated using COMSOL Multiphysics software (open symbols). The FEM results are based on the same flow equations and hard-sphere transport properties underlying the mBLA method. Details of the employed FEM model are given in the work by Park and Nägele.[22]

For C1 conditions, the surface concentration profile $\phi_w(z)$ of non-cake-forming systems increases monotonically with increasing axial distance z from the inlet (see the left panel). The increase is more pronounced for larger TMP^0, as expected. The radial concentration profile, $\phi(y, z = L)$, depicted in the right panel of Fig. 4 decays in a nonexponential fashion with increasing y. According to Eq. (37) for the matched asymptotic solution for $\phi(y, z)$, a purely exponential decay in y is recovered for constant transport properties and zero shear only, for which the film theory prediction of exponential decay is recovered.[7] As expected, the strength and range of the radial profile $\phi(y, L)$ at the outlet increases with increasing TMP^0 due to enlarged advection of particles toward the membrane surface. The left panel of Fig. 5 displays mBLA results for the channel-length-averaged permeate flux, $\langle v_w \rangle_L$, of hard-sphere dispersions of varying particle radius a, in the range from 3.13 nm matching the mean size of globular bovine serum albumin proteins[52] up to 100 nm. The linear solid line holds for pure solvent, where the crossflow setup attains the maximal mean permeate flux $\langle v_w \rangle_L = L_P^0\ \mathrm{TMP}^0$ growing linearly in TMP^0. For $a = 3.13$ nm, the osmotic pressure of the feed dispersion at $\phi_b = 10^{-3}$ is about 30 Pa, according to the Carnahan–Starling pressure Eq. (13) and $k_B T/V_a \approx 30$ kPa. For small particles where Brownian motion is strong and the osmotic pressure is accordingly strong, even a small increment in ϕ_w significantly lowers the permeate flux, causing in the low-TMP^0 region in the curve of $\langle v_w \rangle_L$ for $a = 3.13$ nm to be located slightly below the one for $a = 10$ nm. No cake is predicted for $a = 3.13$ nm, owing to the strong osmotic pressure contribution in the Darcy–Starling boundary condition. For the larger radius $a = 10$ nm, where the osmotic pressure at ϕ_b is only about 1 Pa (since, here, $k_B T/V_a \approx 1$ kPa), the initial deviation from the pure-solvent solid line is less pronounced than for $a = 3.13$ nm. However, a cake layer is now formed, initially at $z = L$, once a TMP^0 value of about 8.17 kPa is exceeded (see the open circle). This TMP^0 value is larger than the osmotic

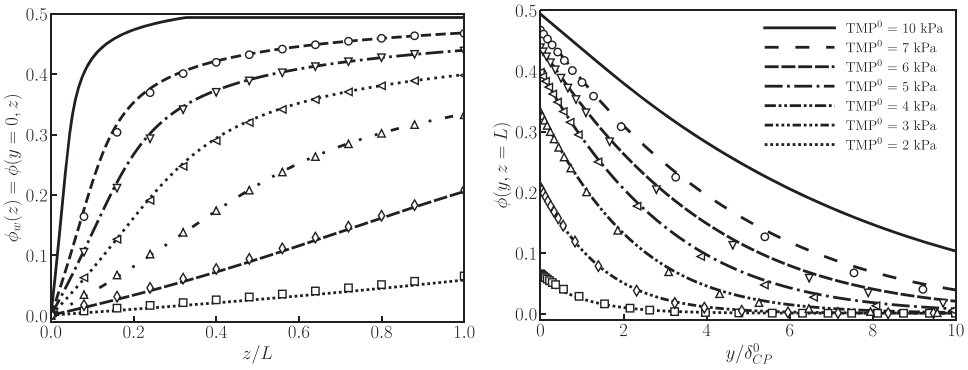

FIG. 4. Left panel: CP layer axial wall-concentration profile $\phi_w(z) = \phi(y = 0, z)$; right panel: radial profile $\phi(y, z = L)$ at the outlet, for the UF set C1, using $a = 10$ nm and TMP^0 values listed. The curves denote mBLA predictions, and the symbols denote finite elements (FEM) calculation results. The radial distance, y, from the membrane surface is measured in units of the characteristic CP layer thickness, $\delta^0_{CP} = R\,\varepsilon$.

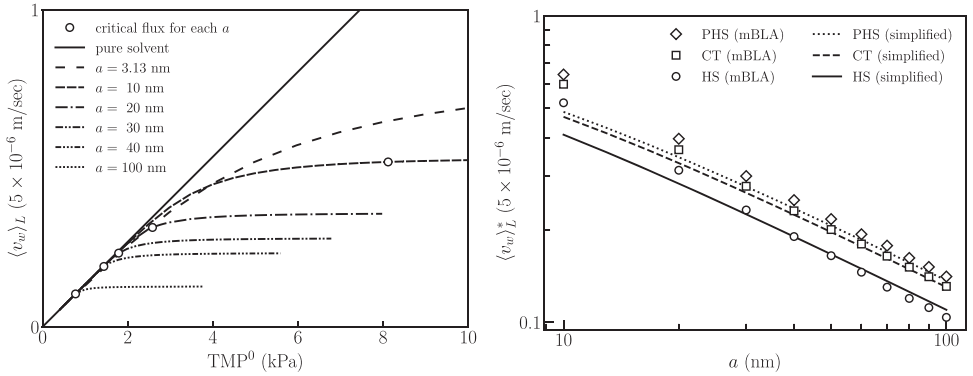

FIG. 5. Left panel: mBLA results for the length-averaged mean permeate flux, $\langle v_w \rangle_L$, as a function of characteristic TMP^0, for parameter set C1 and various particle radii a as indicated. The open circles mark the minimal (critical) TMP^0, for given a, where a cake layer appears first at the outlet, i.e., where $\phi_w(z = L) = \phi_f$ for $\phi_f = 0.494$. Right panel: Log–log plot of the critical mean permeate flux, $\langle v_w \rangle^*_L$, as a function of a, for three different particulate systems under C1 conditions, namely, hard spheres (HS), hypothetical hard spheres with constant transport properties identified as their infinite dilution values (CT), and solvent-permeable hard spheres (PHS). The open symbols denote mBLA results. The lines denote predictions from a simplified critical flux calculation that neglects osmotic pressure, as explained in the main text.

pressure at freezing concentration, which for $a = 10$ nm is given by $\Pi^{eq}(\phi_f) \approx 6.2$ kPa.

The open circles in the left panel of Fig. 5 mark the critical (mean) permeate flux, $\langle v_w \rangle^*_L$, and its associated critical TMP^{0,*} values, indicated by an asterisk, where a cake shows up first at the outlet, owing to the monotonic axial growth of $\phi_w(z)$ under C1 and C2 conditions with $\phi_w(z < L) < \phi_w(L)$. Recall that according to the mBLA scheme, a cake is present at all z values where the threshold value $\phi_w(z) = \phi_f$ is reached. With further increasing TMP^0 above the onset value of cake formation, the cake is stretching out from the outlet position into the interior of the channel toward smaller positions z with $z_c \le z < L$. This is coupled to an accordingly attenuated growth of $\langle v_w \rangle_L$ above the critical flux value, as it is noticed in the figure. For very large TMP^0 values, an apparent so-called limiting flux behavior is observed where $\langle v_w \rangle_L$ becomes insensitive to changes in the transmembrane pressure. The critical flux (open circles) decreases with increasing radius, and for $a > 20$ nm, it approaches the pure-solvent line, indicating a diminishing influence of the CP layer generated by back diffusion of particles away from the inner membrane or cake surfaces. The left panel of Fig. 5 further illustrates for $a = 20$ nm that the critical permeate flux, below which no cake appears, can differ distinctly from the mean flux value where the mean flux vs TMP^0 curve is about to deviate from the linear pure solvent line.

In the right panel of Fig. 5, the critical flux $\langle v_w \rangle^*_L$ is shown on a double logarithmic scale as a function of the particle radius. The mBLA predictions (open symbols) are displayed for three different types of particulate systems under C1 conditions of negligible shear, namely, first for hard spheres (HS) with concentration-dependent viscosity and radial diffusion coefficient given in Sec. II C, second a reference dispersion labeled by CT (constant transport properties) for which the infinite dilution values $\eta = \eta_s$ and $D_{yy} = D_0$ are used but the hard-sphere osmotic pressure contribution is still accounted for, and third a system of porous hard spheres which are uniformly solvent permeable. As described in Refs. 22 and 30, a solvent-permeable hard sphere behaves hydrodynamically as a no-slip hard sphere with a hydrodynamic radius, a_h, smaller than its hard-core radius a. The transport coefficients without shear, $D_{yy}(\phi, \gamma)$ and $\eta(\phi, \gamma)$, depend on the ratio $\gamma = a_h/a$ in addition to ϕ, and they account for increasing radial diffusion (decreasing viscosity) with decreasing γ. The critical flux curve for the permeable hard spheres (PHS) system shown in the right panel is obtained using $\gamma = 0.9$, corresponding to distinctly enlarged radial diffusion (distinctly reduced viscosity) compared to a HS sys-

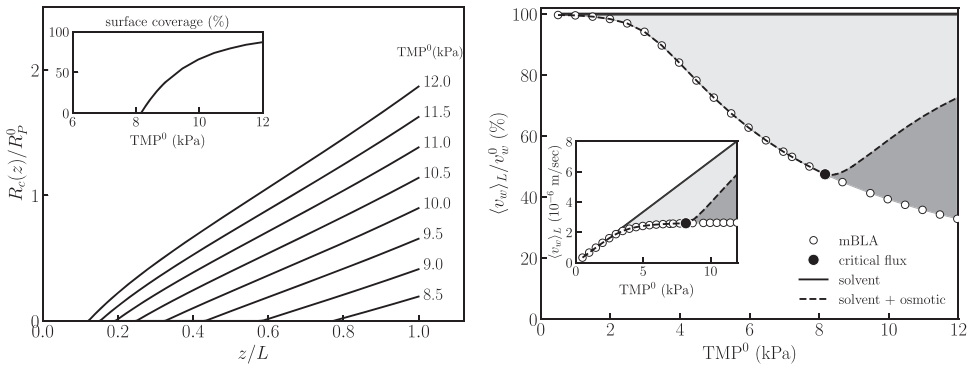

FIG. 6. Influence of the cake layer on hydraulic permeability and filtration efficiency of the CF setup, for parameter set C1 and a = 10 nm. Left panel: reduced hydraulic resistance profile, $R_c(z)/R_P^0$, for TMP^0 values, as indicated. The inset gives the fraction of the membrane surface covered by the cake layer. Right panel: filtration efficiency, $\langle v_w\rangle_L/v_w^0$, vs TMP^0. The circles denote efficiency values predicted by using the mBLA method. The filled circle marks the efficiency at critical TMP^{0,*} = 8.17 kPa. The dashed curve denotes the pure solvent plus osmotic pressure contribution, $1 - \langle L_P(z)\ \Pi^{eq}(\phi_w(z))\rangle_L/v_w^0$, to the filtration efficiency. The inset depicts the mean permeate flux $\langle v_w\rangle_L$ in its absolute unit.

tem of non-permeable hard spheres at the same ϕ where $\gamma = 1$. The employed analytic expressions for $D_{yy}(\phi,\gamma)$ and $\eta(\phi,\gamma)$ of the PHS system are given by Park and Nägele.[22] The larger diffusivity and smaller viscosity of the PHS system give rise to a larger critical flux for initial cake formation, clearly visible in the figure. We do not dwell here on permeable particle systems, whose consideration in the figure serves only to illustrate that the mBLA method is readily applicable to dispersions of hydrodynamically structured particles, such as non-ionic microgels. Critical flux values of HS dispersion are smaller than those of the corresponding CT systems, exemplifying that the effect of increased viscosity $\eta > \eta_s$ for non-zero concentration outweighs that of an enlarged radial diffusion coefficient $D_{yy} > D_0$.

The depicted mBLA results for the critical flux of the three considered particulate systems (open symbols) should be compared with a simplified analysis of the mBLA equations in Sec. IV, where the osmotic pressure contribution is disregarded and the analytical flow profiles of pure solvent given by Park and Nägele[22] are used. This results in a simplified expression for $\langle v_w\rangle_L^*$ given in Eq. (50), where $G(L)^*$ is given analytically by Eq. (47) for $z = L$ under critical flux conditions and $\Psi(L)^*$ is determined from a numerical integration with respect to y.

The simplified expression for $\langle v_w\rangle_L^*$ in Eq. (50) gives rise to the approximately linearly decreasing curves shown in the right panel of Fig. 5. It becomes more accurate for larger particles with lower osmotic pressure, as shown in the figure. When the dispersion flow is approximated by a Hagen–Poiseuille flow, the scaling relation $\langle v_w\rangle_L^* \propto a^{-2/3}$ is obtained. This scaling relation for Brownian particles is also predicted by film theory.[8] We recall that in the UF to MF transition regime of small to moderately large Péclet numbers, D_{yy} is proportional to k_BT/a. This behavior is qualitatively different from the MF regime of large non-Brownian particles, where the athermal, shear-induced hydrodynamic diffusion coefficient scales as $D_{yy}^{hyd} \propto a^2$.

For parameter set C1 and a = 10 nm, the left panel of Fig. 6 shows the effect of the cake layer on filtration in terms of the (reduced) cake hydraulic resistance profile, $R_c(z)/R_P^0$, given in Eq. (8), and in terms of the cake surface coverage $(L - z_c)/L$ of the membrane (inset), as a function of z and TMP^0, respectively. According to the mBLA scheme, no cake is formed for $0 \le z < z_c$, whereas a thin cake is present for $z_c \le z \le L$. The axial width, $L - z_c$, of the cake expands monotonically under C1 conditions with increasing TMP^0, with a surface coverage $(L - z_c)/L$ of 75% for TMP^0 = 12 kPa (see the inset). For smaller TMP^0 < 8.3 kPa, no cake layer is predicted, reflected by vanishing surface coverage. Except near to $z \approx z_c$, the hydraulic resistance $R_c(z)$ of the cake grows approximately linearly in z, which according to Eq. (8) implies an approximately hyperbolic axial decay of the hydraulic permeability profile, $L_P(z)$, for increasing z.

The right panel of Fig. 6 displays the filtration efficiency, $\langle v_w\rangle_L/v_w^0$, vs TMP^0 = v_w^0/L_P^0. The maximum efficiency of 100% is obtained for pure solvent feed where $\langle v_w\rangle_L = v_w^0$, represented by the solid line in the inset with slope 1. Note that the inset depicts the non-normalized mean permeate flux. The open circles denote efficiency values predicted by using the mBLA method. The filled circle denotes the efficiency value at the critical TMP^0 value of 8.17 kPa, below which no cake is formed. The dashed curve represents the pure solvent plus osmotic pressure contribution, $1 - \langle L_P(z)\ \Pi^{eq}(\phi_w(z))\rangle_L/v_w^0$, to the filtration efficiency. This contribution equals the full filtration efficiency for subcritical TMP^0 values where no cake is formed and where the efficiency decreases with increasing subcritical TMP^0 values, owing to the increasing osmotic pressure at the membrane surface for constant $L_P(z) = L_P^0$. In contrast, it increases for increasing TMP^0 larger than the critical one since $L_P(z)$ decreases here with increasing cake formation, while the osmotic pressure at the cake surface remains constant equal to $\Pi^{eq}(\phi_f)$.

B. Shear effects on the CP layer and cake formation

We proceed by discussing mBLA results for the parameter set C2. Here, the influence of shear on CP and cake layers comes into play through significant shear-induced enhancement of $D_{yy}(\phi, Pe_a)$ given in Eq. (14) and shear-induced thinning of $\eta(\phi,\tilde{\tau})$ modeled for colloidal hard spheres by the empirical Williams expression

in Eq. (11). Regarding osmotic pressure, the Carnahan–Starling expression in Eq. (13) for zero shear is used, as discussed in the context of this equation. As noticed in Table I, for set C2, the hydraulic membrane mobility L_P^0 is three orders of magnitude larger, and the central inlet flow velocity u^0 is two orders of magnitude larger than the corresponding values for set C1. As our mBLA calculations show, the Péclet numbers of set C2 re-scaled by the local viscosity at the cake surface, i.e., $Pe_a^f = Pe_a^0/(\eta(\phi_f,0)/\eta_s)$, are of $\mathcal{O}[1]$, reaffirming that the above noted expressions for D_{yy} and η can be used.

The local Péclet number, $Pe_a(y,z)$ entering $D_{yy}(\phi, Pe_a)$ and the mBLA solutions for the concentration and flow profiles, follows from Eq. (31) combined with Eq. (38) for the asymptotically matched $u(y,z)$. To leading order in ε, it is given by

$$Pe_a(y,z) \approx \frac{Pe_a^0}{2}\frac{u(R,z)}{u^0}\left[\frac{2-y/R}{\eta(\phi(y,z),\tilde{\tau}(z))/\eta_s} - \frac{1}{R}\int_0^y \frac{1}{\eta(\phi(y',z),\tilde{\tau}(z))/\eta_s}dy'\right], \tag{51}$$

with $Pe_a(0,0) = Pe_a^0$. The axial profile of the local Péclet number at the inner membrane (cake) surface follows as

$$Pe_a(0,z) \approx Pe_a^0\,\frac{u(R,z)/u^0}{\eta_w(z)/\eta_s}, \tag{52}$$

where $\eta_w(z) = \eta(\phi_w(z),\tilde{\tau}(z))$ is the dispersion viscosity at the inner membrane or thin cake surface at $y = 0$. As predicted by the mBLA method in thin cake approximation for both sets C1 and C2, $\phi_w(z)$ is monotonically increasing and $Pe_a(0,z)$ is monotonically decreasing axially along the channel length L. Using the Williams viscosity expression in the mBLA calculations for small Pe_a^0, one finds $\eta_w(z_c \le z \le L)/\eta_s \approx 21$, i.e., a distinctly enlarged viscosity at the cake surface.

The local shear stress, $\tau(y,z) = \eta(y,z)\partial u(y,z)/\partial y$, inside the CP layer is according to Eq. (32) a function of z only. Therefore,

$$\tilde{\tau}(z) \approx \frac{Pe_a^0}{6\pi\, b}\,\frac{u(R,z)}{u^0}, \tag{53}$$

to leading order in ε, with inlet stress value $\tilde{\tau}(z=0) \approx Pe_a^0/(6\pi\, b)$. Since $u(R,z) = -(R^2/4\eta_s)dP(z)/dz$ according to Eq. (25), the reduced shear stress of the CP layer decreases monotonically in axial direction, well below its maximal value $Pe_a^0/(6\pi b)$ taken at the inlet wall where $z = 0$.

In the left panel of Fig. 7, the wall concentration profile $\phi_w(z)$ of C2 systems is shown for fixed $\mathrm{TMP}^0 = 1.5$ kPa and particle radii $a = 100, 150, 200$ nm. The lines represent mBLA results where shear-enhanced radial diffusion and viscosity shear-thinning are accounted for using $D_{yy}(\phi, Pe_a)$ given in Eq. (14) and $\eta(\phi\tilde{\tau})$ in Eq. (11). The influence of shear flow is assessed quantitatively by comparison with mBLA concentration profiles (open symbols) for a reference system where the zero-shear equilibrium expressions $D_{yy}(\phi, Pe_a = 0)$ and $\eta(\phi, \tilde{\tau} = 0)$ are used as input. Shear-induced enhancement of radial diffusion and viscosity shear-thinning leads to less developed CP layers, disfavoring cake formation. Compared to the unsheared reference systems, the entrance length, z_c, of the cake layer [for which $\phi_w(z > z_c) = \phi_f$] is shifted to larger values (smaller surface coverage) and the values for the hydraulic cake resistance $R_c(z)$ are accordingly smaller. Primarily due to the size scaling $D_{yy} \propto 1/a$, cake formation is enhanced for less mobile larger particles, reflected by an accordingly larger cake surface coverage (i.e., a smaller z_c-value).

The right panel of Fig. 7 displays the radial CP layer concentration profile, $\phi(y,L)$, at the outlet port, for the same TMP^0 value and particle radii as in the left panel. Since a thin cake is present at the outlet where its surface is at $y = 0$, it holds $\phi(0,L) = \phi_w(L) = \phi_f$, where $\phi_f = 0.494$. For all a values, the radial profile converges to the bulk concentration $\phi_b = 10^{-5}$ when $y > 10\ \delta_C^0$. Using $\delta_{CP}^0 = R/Pe_R$, where $Pe_R = 3500$ and $Pe_R = 7000$ for $a = 100$ and 200 nm, respectively, the radial distance $y = 10\ \delta_{CP}^0$ from the membrane wall amounts to only 0.29% and 0.14% of the inner channel radius R, respectively, underscoring the applicability of the employed boundary layer description. Consistent with the axial

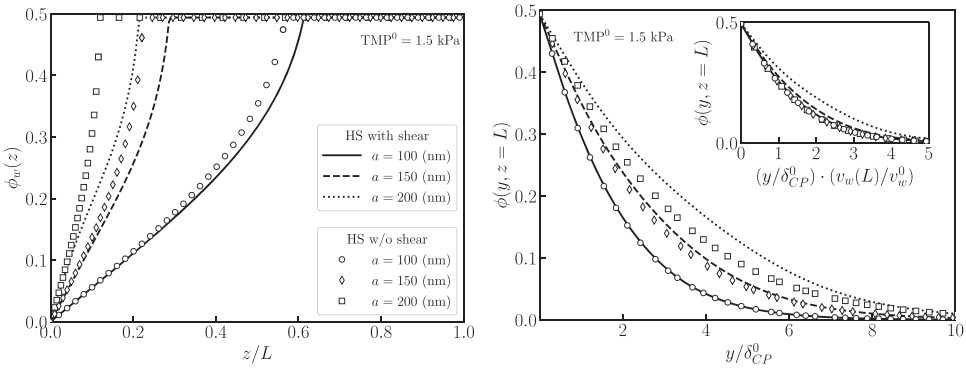

FIG. 7. Left panel shows the axial and the right panel shows the radial CP layer concentration profiles, $\phi_w(z)$ and $\phi(y,L)$, respectively, for parameter set C2 and particle radii a, as indicated. The applied TMP^0 is fixed to 1.5 kPa. The lines denote mBLA results where shear-enhanced diffusion and viscosity thinning are accounted for, while the open symbols represent mBLA results for a reference system where the constant, zero-concentration values for D_{yy} and η are used (i.e., $\phi = 0$, $Pe_a^0 = 0$, and $\tilde{\tau} = 0$). Radial distance y is scaled by the characteristic CP layer thickness $\delta_{CP}^0 = \varepsilon\ R$ and in the inset, it is scaled by $\delta_{CP}^0\ v_w^0/v_w(L)$.

profile $\phi_w(z)$, the radial profile $\phi(y,L)$ at the outlet is more pronounced and broader for the less mobile, larger particles. In comparison with the HS system, where shear flow is disregarded (open symbols), the particles are more mobile and diffuse more easily away from the membrane (cake) surface when viscosity thinning (see Fig. 2) and shear-enhanced radial diffusion (see Fig. 3) are accounted for, reflected in the broader concentration profiles (lines). For $a = 100$ nm, however, the radial concentration profiles at the outlet, with and without shear, are practically coincident. This can be attributed to the characteristic Péclet number $Pe_a^0 = 3.7$ for the $a = 100$ nm particles, which is small compared to the Péclet number 29.6 for the $a = 200$ nm spheres. In fact, since the radial profiles are considered here right at the outlet where the cake of volume fraction ϕ_f is present, instead of Pe_a^0, one should consider the viscosity-rescaled characteristic Péclet number defined by $Pe_a^f = Pe_a^0/\big(\eta_0(\phi_f)/\eta_s\big)$ for which $Pe_a^f = 0.17$ and 1.37 for $a = 100$ and 200 nm, respectively. The inlet displays the radial profiles as functions of y/δ_{CP}^0 multiplied by the non-dimensionalized outlet permeate flux $v_w(L)/v_w^0$. The profiles without shear (open symbols) coincide in this representation since, according to Eq. (14), the $1/a$ scaling of $D_{yy}(\phi, Pe_a = 0)$ is canceled by the according scaling of $1/D_0$ and since $\phi_w(L) = \phi_f$ due to the presence of the cake.

The left panel of Fig. 8 displays the CP layer radial Péclet number profile, $Pe_a(y, z = L) = (a^2/D_0)\partial u(y,L)/\partial y$, at the outlet as a function of the reduced radial distance $y/\delta_{CP}^0 \lesssim 10$. The complete profile, including the broad bulk region outside the CP layer, is depicted in the inset, now in dependence on y/R. Hard spheres (HS) of two different particle radii $a = \{100, 200\}$ nm are considered, and mBLA results with shear (lines) and without shear (open symbols) are shown, together with the corresponding results for a reference system (labeled CT) with constant transport properties, $D_{yy} = D_0$ and $\eta_s = \eta_0$, where osmotic pressure effects are still accounted for. The radial profiles of the reduced axial velocity at the outlet, $U(y) = u(y, z = L)/u(R,L)$, multiplied by the CP-layer stretching factor $1/\varepsilon = R/\delta_{CP}^0$, are shown in the right panel. The unstretched velocity profiles $U(y)$ in the full radial range of the channel are shown in the inset, now as functions of y/R. For both radii and all considered cases (i.e., HS systems with and without shear, and CT systems), a cake is formed at the outlet so that $\phi_w(L) = \phi_f$.

According to the mBLA analysis in Sec. III, only the radial variation of the axial velocity u is affected by the presence of a CP layer, whereas the radial velocity component v is y-independent inside the layer. In the bulk region of the dispersion outside the CP layer, the reduced axial velocity, $u(y,z)/u(y,R)$, is, according to Eq. (25), practically equal to the quadratic HP profile, $u_{HP}(z)/u^0$, given in Eq. (6). In particular, $u(y,L)/u(R,L) \approx 1 - (1 - y/R)^2$, where $u(R,L) = -(R^2/4\eta_s)P'(z = L)$ holds in the bulk region of the outlet. Hence, $Pe_a(y, z = L) \approx Pe_a^0\big(u(R,L)/u^0\big)(1 - y/R)$ decays linearly in the bulk region. Owing to the axisymmetry, $Pe_a(y = R, z) = 0$ holds exactly, which explains the steep decline of $Pe_a(y,L)$ toward zero value for $y \to R$, visible on the double logarithmic scale of the left panel. Significant deviations from the quadratic HP profile for $U(y)$, and the linear HP profile for $Pe_a(y,L)$ are manifested in the thin CP layer only, originating from the concentration dependence of $\eta(\phi,\tilde{\tau})$. As noticed from the inset in the left panel, for HS systems with shear (lines) and without shear (open symbols), the latter are obtained using $D_{yy} = D_{yy}(\phi, Pe_a = 0)$ and $\eta = \eta(\phi, \tilde{\tau} = 0)$, and the corresponding profiles of $Pe_a(y,L)$ are not any more linearly deceasing functions in y. Instead of having its largest value at $y = 0$, $Pe_a(y,L)$ attains its maximum in the transition region between the CP layer and bulk phase. It increases monotonically in the CP layer, more strongly so for the larger 200 nm particles since $a^2/D_0 \propto a^3$. The radial gradient of Pe_a inside the CP layer follows for $y \ll R$ from Eq. (51) as

$$\frac{\partial Pe_a(y,z)}{\partial y} \approx -Pe_a^0\,\frac{u(R,z)}{u^0}\,\frac{\eta_s}{\eta(\phi,\tilde{\tau})^2}\,\frac{\partial \eta(\phi,\tilde{\tau})}{\partial y}. \tag{54}$$

The radial profile $\phi(y,L)$ is monotonically decreasing with increasing y toward its small bulk value ϕ_b. In conjunction with the y-independence of $\tilde{\tau} = \tilde{\tau}(z)$, this leads to a monotonic radial decay of

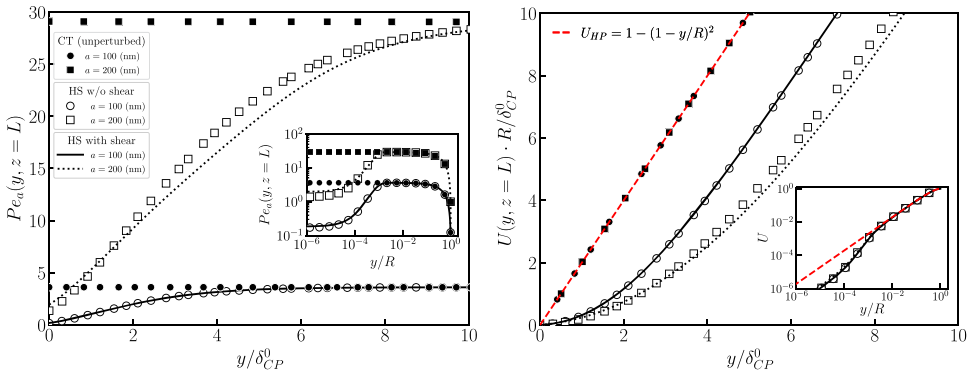

FIG. 8. left panel shows the radial Péclet number profile, $Pe_a(y, z = L)$ and the right panel shows the radial profile of the normalized axial velocity, $U(y) = u(y,L)/u(R,L)$, multiplied by the stretching factor $R/\delta_{CP}^0 = 1/\varepsilon$, as functions of radial distance y/δ_{CP}^0. Parameters are those of set C2. The solid and dotted lines (open circles and squares) are mBLA results for hard spheres (HS) with (without) shear, for $a = 100$ and 200 nm, respectively. The filled symbols represent mBLA results for constant transport properties $D_{yy} = D_0$ and $\eta = \eta_s$ but non-zero osmotic pressure (CT). Inset in the left panel: Log–log plot of $Pe_a(y, z = L)$ in full radial range R. The dashed line in the right panel depicts the Hagen–Poiseuille flow profile $U_{HP}(y)$. The inset in the right panel displays $U(y)$ vs y/R for the HS system with shear.

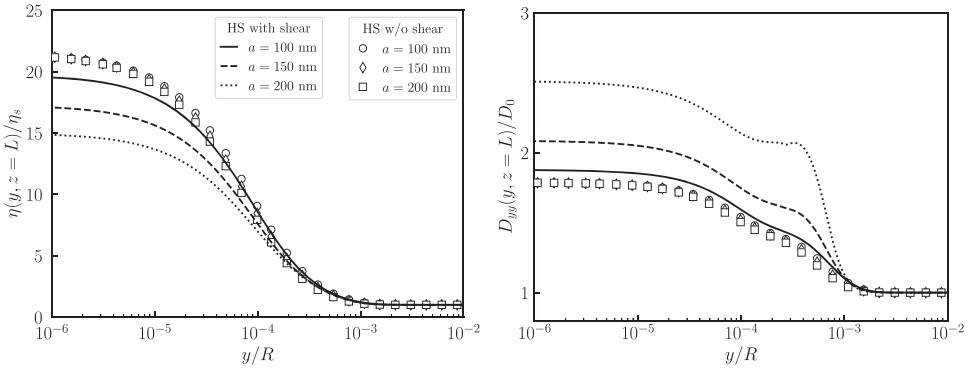

FIG. 9. Radial profiles of the reduced dispersion viscosity $\eta(y,L)/\eta_s$ (left) and the reduced radial diffusion coefficient $D_{yy}(y,L)/D_0$ (right) at the outlet cross-section, as functions of y/R. The values of radius a as shown in Fig. 7 are considered.

$\eta(\phi,\tilde{\tau})$, i.e., $\partial\eta/\partial y < 0$ holds in the CP layer (also see Fig. 9), which leads to the monotonic growth of $Pe_a(y,L)$ inside the CP layer visible in the figure.

The y-dependence of the viscosity inside the CP layer causes a smaller growth of $U(y)$, above its value $U(y=0)=0$ at the cake surface (see the inset in the right panel), than described by $U_{HP}(y)$, which is represented by the red dashed line in the right panel. The viscosity-induced perturbation of $U(y)$ away from $U_{HP}(y)$ is more pronounced for the larger particles. The perturbation is weakened, however, by viscosity shear-thinning, giving rise to smaller $Pe_a(y,L)$ values than without shear (cf. open squares and dotted lines in both panels). In contrast, for the smaller 100 nm particles, the effect of shear-thinning on $Pe_a(y,L)$ and $U(y,L)$ is negligible since the corresponding Pe_a values are distinctly smaller than those of the larger particles (solid lines and open circles). The Pe_a and U profiles of the HS systems with and without shear converge toward the corresponding HP profiles in the bulk region, where $y/R \gg 10^{-2} \sim 10\delta_{CP}/R$ (see both the insets). In comparison, for the CT reference system where the viscosity is equal to $\eta_s \approx \eta(\phi_b,\tilde{\tau})$, the radial Péclet number and axial velocity profiles (filled symbols) are also of Hagen–Poiseuille form inside the CP layer. For $y/\delta^0_{CP} < 10$, the CT reference system reduced shear-rate profiles are practically constant and equal to $Pe_a^{CT}(y,L) = 2a^2 u_{CT}(R,L)/(R\,D_0)$. Owing to the small feed concentration, $\phi_b = 10^{-5}$, the bulk values of Pe_a are practically the same for the HS and CT systems.

Figure 9 displays the mBLA radial profiles for the reduced dispersion viscosity, $\eta(y,L)/\eta_s$ (left panel), and reduced radial diffusion viscosity, $D_{yy}(y,L)/D_0$ (right panel), both taken at the outlet cross section $z = L$. A logarithmic distance scale is used for y to encompass the CP layer and the transition region into the bulk. Notice here that $\varepsilon = 2\times10^{-3}$ and 10^{-3} for $a = 100$ and 200 nm, respectively. Both η/η_s and D_{yy}/D_0 decrease monotonically with increasing radial distance y from the cake layer surface at $y = 0$ toward a common value 1 since $\eta \approx \eta_s$ and $D_{yy} \approx D_0$ in the bulk region where $\phi = \phi_b \ll 1$. For hard spheres without shear (open symbols), there is practically no particle size dependence of the two reduced transport properties, consistent with the size-independence of the corresponding radial concentration profiles $\phi(y,L)$ without shear, with $\phi(y=0,L) = \phi_f$, as shown in the right panel of Fig. 7. The (explicit) dependence $D_{yy} \propto 1/a$ according to Eq. (14) is canceled out by the corresponding dependence of D_0 in the curves of D_{yy}/D_0 shown in the right panel. In regards to $\eta(\phi(y,L),\tilde{\tau}(y,L))$, the shear stress on which it depends is y-independent inside the CP layer and equal to its value at the cake surface $y = 0$.

For HS systems where shear-thinning and shear-enhanced diffusion effects are accounted for (lines), increasing a increases Pe_a, which, in turn, causes stronger shear-thinning (see Fig. 8, left panel). For a given ϕ, viscosity shear-thinning is stronger for larger particles since these are less affected by Brownian motion. Notice here that the Williams viscosity expression in Eq. (11) describing shear thinning has an explicit particle-size-dependence due to the thermal stress τ_{th}. As seen in the figure, shear-induced enhancement of D_{yy}/D_0 is likewise more pronounced for larger particles, where $Pe_a(y,L)$ and $\phi(y,L)$ are larger than without shear. For the $a = 100$ nm particles (solid lines), shear-induced effects are small, reflected in a small viscosity reduction and radial diffusion enhancement away from the zero-shear case. In contrast, shear thinning and shear-enhanced Brownian diffusion are pronounced for the $a = 200$ nm spheres.

In the right panel of Fig. 9, a shallow secondary maximum of D_{yy}/D_0 is seen at $y/R \sim 10^{-3}$ for the $a = 200$ nm particles. The corresponding Péclet number $Pe_a(y,L) \sim 30$ is, however, outside the range of values ($\lesssim 10$) where Eq. (14) can be safely used. For even larger Péclet numbers, one has to account for the disregarded shear-induced migration flux contribution, $-\boldsymbol{\xi}\cdot\dot{\gamma}$, in Eq. (3), and at larger concentrations for shear-thickening effects in case of hard spheres with stick hydrodynamic boundary conditions. An extension of the mBLA method to large Pe_a numbers can be the task of future work.

Figure 10 depicts the mBLA critical flux for hard spheres (HS) under C2 conditions, both with shear (filled circles) and without shear (open circles), in its dependence on $a \in [20\text{–}200]$ nm. The critical flux indicates $\langle v_w\rangle^*_L$ for the $a = 200$ nm particles, the onset of cake formation at the channel outlet. On the double-logarithmic scale of the figure, the mBLA flux data without shear follow, to good accuracy, the scaling relation $\langle v_w\rangle^*_L \propto a^{-2/3}$. The solid line on which the data points without shear (filled circles) are located to good accuaracy reflects the simplified critical flux expression in Eq. (50), with the critical mass transfer coefficient approximated by $K^*_m = K^0_m$ for K^0_m according to Eq. (48), $A \approx 0.81$ and $D_{yy} = D_0 \propto k_BT/a$, such that $\langle v_w\rangle^*_L \propto a^{-2/3}$. It has been used here that $A = \left(\Psi^*(L)/G^*(L)\right)^{1/3} \approx 0.81$, as obtained from the mBLA solution at the critical TMP^0, where the cake is initially formed at

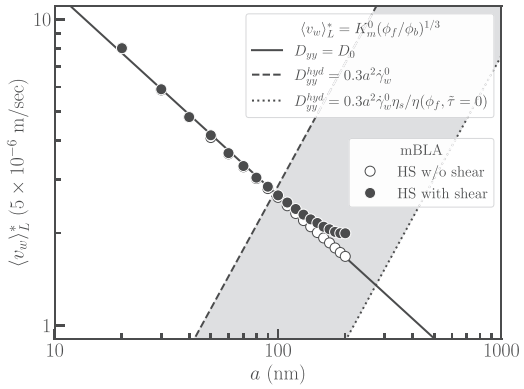

FIG. 10. Critical permeate flux, $\langle v_w \rangle_L^*$, of hard spheres (HS) under C2 conditions, without shear (open circles) and with shear (filled circles). The solid line pictures the simplified flux expression in Eq. (50) for $K_m^* = K_m^0$ according to Eq. (48), with $A = 0.81$ and $D_{yy} = D_0 \propto k_BT/a$ such that $\langle v_w \rangle_L^* \propto a^{-2/3}$. The dashed and dotted lines limiting the tilted slab depict Eq. (50) for $K_m^* = K_m^0$, using $A = 0.81$ and D_0 replaced $D_{yy}^{hyd} = 0.3a^2\dot{\gamma}_w^0$ (dashed) and $D_{yy}^{hyd} = 0.3a^2\dot{\gamma}_w^0\eta_s/\eta(\phi_f, \tilde{\tau} = 0)$ (dotted), respectively.

$z = L$. Shear-enhanced Brownian diffusion and viscosity-thinning cause the colloidal hard spheres in the CP layer to be more mobile than without shear. Consequently, a cake layer is formed only at larger critical TMP^0 and larger $\langle v_w \rangle_L^*$ values than without shear. The shear-induced up-swing of $\langle v_w \rangle_L^*$, noticed from the figure, is located distinctly above the $a^{-2/3}$ scaling form (solid line). It occurs when the viscosity-rescaled Péclet number $Pe_a^f = Pe_a^0\eta_s/\eta(\phi_f, \tilde{\tau} = 0)$ exceeds roughly the value 0.2. Here, $\eta(\phi_f, \tilde{\tau} = 0)/\eta_s = \left(1 - \phi_f/0.63\right)^{-2} \approx 21.46$, according to the Williams viscosity expression in Eq. (11) taken for zero shear stress. In fact, for $a = \{10, 100, 200\}$ nm, the bare and viscosity-rescaled characteristic Péclet numbers are $Pe_a^0 = \{3.7 \times 10^{-3},\ 3.7,\ 30\}$ and $Pe_a^f = \{1.7 \times 10^{-4},\ 0.17,\ 1.4\}$, respectively.

As noted in the final paragraph of Sec. II, for high shear rates and particle radii $a \sim 0.3$–$15\ \mu$m representative of the MF regime, shear-induced hydrodynamic diffusion is important while Brownian diffusion is negligibly small in comparison. Instead of $D_{yy} \propto k_BT/a$ given in Eq. (14), one should use the athermal shear-induced hydrodynamic radial diffusion coefficient $D_{yy}^{hyd} = a^2\dot{\gamma}_w^0 f(\phi)$, for which expressions of its concentration-dependent factor $f(\phi)$ are summarized, e.g., by Vollebregt *et al.*[53] While crossflow MF of large non-Brownian particles is not the topic of this paper, we briefly comment on the expected size-scaling of the critical flux when shear-induced hydrodynamic diffusion dominates the back transport of particles away from the membrane or cake surfaces. For this purpose, we use Eq. (50) for $\langle v_w \rangle_L^*$, with the mass transfer coefficient approximated by $K_m^* \approx K_m^0 = A(\dot{\gamma}^0\ (D_{yy}^{hyd})^2/L)^{1/3}$ akin to Eq. (48), but with D_0 replaced by D_{yy}^{hyd}. Consistent with the constant transport properties approximation underlying Eq. (48), usage of the constant Eckstein expression $D_{yy}^{hyd} = 0.3\ a^2\dot{\gamma}_w^0$ for the characteristic shear-induced diffusion coefficient leads to the scaling relation $\langle v_w \rangle_L^* \propto a^{4/3}$. This scaling differs qualitatively from the $a^{-2/3}$ scaling observed for dominating Brownian diffusion, where $D_{yy} \propto k_BT/a$. The curves for $\langle v_w \rangle_L^*(a)$ in this approximation are straight lines of slope 4/3 on the double-logarithmic scale of the figure. The dashed line is obtained using the bare Eckstein diffusion coefficient, while the dotted line is obtained using the viscosity-rescaled (local) Eckstein coefficient in which $\dot{\gamma}_w \propto Pe_a^0$ is replaced by $\dot{\gamma}_w\ \eta_s/\eta(\phi_f, \tilde{\tau} = 0) \propto Pe_a^f$. For both lines, the same coefficient $A \approx 0.81$ is used as in the Brownian diffusion case (solid line). The tilted shaded stripe, bounded by the dashed and dotted lines, marks the UF to MF transition region. We do not dwell further on MF here. For its detailed description, one needs to account for physical features in addition to shear-induced diffusion, namely, shear-induced migration, non-equilibrium osmotic pressure contributions, shear-induced compression and melting of the cake layer, and hydrodynamic shear thickening (hydrocluster formation) in the case of particles with stick hydrodynamic boundary conditions. As particle size increases further, shear-induced inertial lift forces come into play, driving particles away from boundaries. In the context of MF, these additional features have been discussed in earlier studies that used simplified CF models.[8]

VI. SUMMARY AND CONCLUSIONS

In this paper, the modified boundary layer (mBLA) method of crossflow filtration (CF) in a membrane channel, developed in earlier studies by Park and Nägele,[22] has been extended to situations where a thin filter cake is formed and to conditions characteristic of the UF to MF transition regime where the CP layer is affected by shear flow in addition to Brownian motion. To the best of our knowledge, this paper presents the first systematic study of inside–out CF in the UF to MF transition regime, using concentration- and shear-rate-dependent analytic expressions for D_{yy} and η that account for both Brownian and shear-induced hydrodynamic forces. Earlier studies on CF focused on the UF regime, where shear effects are negligible, and on the MF regime, where Brownian motion is dominated by shear-induced hydrodynamic effects. Unlike earlier boundary layer analyses of CF, we fully account for correlations between flow and concentration profiles and their interrelationships with dispersion transport properties. The mBLA method results are more accurate than similarity solutions of the CP layer concentration profiles.[22] This paper bridges the gap between fundamental research on shear-affected colloidal dispersion flow and inside–out crossflow filtration as a technologically important process.

Using the extended mBLA method, we have calculated steady-state CF flow and concentration profiles for a model dispersion of monodisperse colloidal hard spheres. Particle sizes were considered in the range from a few up to 200 nm, with characteristic shear-Péclet numbers $Pe_a^0 \lesssim 10$, corresponding to viscosity-rescaled Péclet numbers $Pe_a^f = \mathcal{O}[1]$. The mBLA method extended to this regime involves a shear-rate dependent collective Brownian diffusion coefficient $D_{yy}(\phi, \dot{\gamma})$ and the dispersion viscosity $\eta(\phi, \dot{\gamma})$, for which analytic expressions provided by Jin *et al.*[29] and Krieger[42] are used, respectively. The extended mBLA method accounts for Brownian motion, shear-enhanced Brownian diffusion, and shear thinning of viscosity. Regarding D_{yy}, hydrodynamic interactions between the dispersed particles are accounted for by scaling with the concentration-dependent sedimentation coefficient, $K_{sed}^{eq}(\phi)$, given by Banchio *et al.*[44] Without shear, the equilibrium expression $D_{yy} = K_{sed}^{eq}(\phi)/S^{eq}(0)$ is recovered, where $S^{eq}(0)$ is the Carnahan–Starling expression for the osmotic compressibility

of colloidal hard spheres. For consistency, the Carnahan–Starling expression for the equilibrium osmotic pressure was used in the Darcy–Starling wall boundary condition, relating permeate flux to TMP and osmotic pressure. While this amounts to neglecting the shear-rate dependence of the generalized osmotic pressure, the osmotic pressure influence on the permeate flux is expected to be negligible in the UF to MF transition regime. Regarding $\eta(\phi, \dot{\gamma})$, we have used the empirical Williams viscosity expression, which interpolates between Krieger–Dougherty forms for the zero-shear and infinite-shear viscosities η_0 and η_∞, respectively. The Williams viscosity expression can be conveniently formulated in terms of the shear stress, which remains radially constant across the thin CP layer. As demonstrated in comparison with simplifying mBLA calculations of crossflow where transport properties are kept constant, viscosity thinning and shear-enhanced collective radial diffusion become increasingly important with increasing shear rate and volume fraction. Both hydrodynamic effects tend to improve the filtration performance, e.g., by increasing the critical permeate flux and critical TMP, which are indicators for the onset of cake formation, and by decreasing the cake coverage of the membrane surface.

For simplicity, we have used a minimal description of (reversible) filter cake formation, assuming that the volume fraction of immobilized particles is constant. The cake layer acts as an additional membrane, increasing the hydraulic resistance of the filtration setup. The geometric cake thickness is disregarded in the mBLA calculations, while the increase in the cake hydraulic resistance, $R_c(z)$, with increasing axial distance z from the inlet is accounted for using Ergun's equation describing an ordered fcc array taken at volume fraction $\phi = \phi_f = 0.494$.

A new finding of this paper is the shear-induced non-monotonicity of the radial shear-rate profile, which exhibits a peak at a radial distance y from the membrane/cake surface, located in the CP-bulk transition region. While for the considered parameters and cake model the mBLA concentration profile $\phi_w(z) = \phi(0, z)$ is monotonically increasing, from $\phi_w(0) = \phi_b$ at the inlet up to ϕ_f at axial distances $z_c \le z \le L$ where a thin cake is present, $\phi_w(z)$ can become non-monotonic for a sufficiently large axial particle flux. As a consequence, distinct cake layer ring(s) can be formed. In the UF regime and without cake formation, mBLA results for non-monotonic concentration profiles have been discussed already by Park and Nägele[22] for $\phi_w(z)$ profiles with a maximum at distances $z/L \approx 0.4$–0.5 and wherein a criterion for the occurrence of non-monotonic profiles is given. In future work, it will be beneficial to explore how the non-monotonicity of $\phi_w(z)$ and the corresponding cake layer profiles are affected by shear in the UF to MF transition regime. Moreover, the mBLA method can be further generalized to more refined fouling models for a compressible amorphous cake, irreversible particle adsorption at the membrane surface and clogging of membrane channels.

In the framework of the generalized mBLA scheme, a useful general expression $\langle v_w \rangle_L = K_m (\phi(L)/\phi_b)^{1/3}$ for the mean permeate flux has been provided in Eq. (44), with mass transfer coefficient K_m according to Eq. (45). We have numerically analyzed this expression as a function of the characteristic transmembrane pressure, TMP^0, and particle radius a. The power law concentration dependency is a consequence of cross-sectional particle flux conservation and it differs from the logarithmic $\log(\phi_f/\phi_b)$ dependency of $\langle v_w \rangle_L$ suggested by film theory.[5,8] The latter dependency has been rightfully criticised.[49] At large TMP^0, an (apparent) limiting flux behavior is observed where $\langle v_w \rangle_L$ becomes insensitive to changes in the transmembrane pressure and where most of the membrane is covered by the filter cake. In analyzing the mBLA mean permeate flux expression for constant transport properties and a simplified description of crossflow, an earlier version of the mass transfer coefficient K_m is obtained as a limiting case, but now with a more realistic expression for its prefactor A.

Our calculations of the critical flux as a function of a, for otherwise fixed operating conditions, reveal the well-known power-law decline according to $\langle v_w \rangle_L^* \sim a^{-2/3}$, for small a in the UF regime where Brownian diffusion dominates.[8] With further increasing particle radius, for values $a > 10$ nm, the generalized mBLA theory predicts an upturn of $\langle v_w \rangle_L^*$ significantly above the $a^{-2/3}$ power law prediction, which is due to shear-enhanced Brownian diffusion and shear thinning of viscosity. The upturn starts roughly for viscosity-rescaled Péclet number values $Pe_a^f \approx 0.2$. The observed shear-induced flux upturn adds to the resolution of the (apparent) flux paradox of CF in the UF to MF transition regime. As an aside, for large particles and Péclet numbers, the scaling relation $\langle v_w \rangle_L^* \sim a^{4/3}$ is obtained from the simplified mBLA flux expression, provided D_{yy} is identified by the shear-induced self-diffusion coefficient $D_{yy}^{hyd} \propto a^2 \dot{\gamma}$ of non-Brownian hard spheres as in earlier studies by Eckstein *et al.*[54] and Belfort *et al.*[8]

While this paper is about CF of colloidal hard spheres, the generalized mBLA method can also be applied to dispersions of solvent-permeable particles, such as non-ionic globular microgels, and to dispersions of charge-stabilized colloidal particles, provided appropriately adjusted transport properties are used. An example is shown in the right panel of Fig. 5, which includes the critical flux of solvent-permeable hard spheres (PHS) in addition to that of non-permeable spheres. Particle size polydispersity can be included in the mBLA scheme by accounting for static cross correlations (i.e., partial radial distribution functions) and dynamic cross correlations in the hydrodynamic diffusivities and the dispersion viscosity. In proceeding beyond an effectively one-component treatment of polydispersity as done by Vollebregt *et al.*,[50] a set of advection-diffusion equations needs to be considered in which the concentration fields and fluxes of the various particle components are coupled. Such a multi-component treatment allows for studying size fractionation along the membrane channel. This can be the topic of a future study.

ACKNOWLEDGMENTS

The authors thank M. Brito (University of Stuttgart) for helpful discussions. This work was supported by the Deutsche Forschungsgemeinschaft (former SFB-985, Project No. 191948804, B6).

AUTHOR DECLARATIONS

Conflict of Interest

The authors have no conflicts to disclose.

Author Contributions

Gun Woo Park: Conceptualization (equal); Data curation (equal); Formal analysis (equal); Investigation (equal); Methodology (equal); Software (equal); Validation (equal); Visualization (equal); Writing – original draft (equal); Writing – review & editing (equal). **Jan K. G. Dhont**: Conceptualization (equal); Investigation (equal); Methodology (equal); Writing – original draft (equal); Writing – review & editing (equal). **Gerhard Nägele**: Conceptualization (equal); Funding acquisition (equal); Investigation (equal); Project administration (equal); Writing – original draft (equal); Writing – review & editing (equal).

DATA AVAILABILITY

The data that support the findings of this study are available from the corresponding author upon reasonable request.

APPENDIX A: FIXED-POINT ITERATION FOR WALL CONCENTRATION AND CAKE RESISTANCE

We explain here how the particles' concentration profile at the membrane or cake surface, $\phi_w(z)$, and the hydraulic resistance profile of the cake, $R_c(z)$, are calculated self-consistently for all z values in $[0,L]$, using an under-relaxed fixed-point iteration (FPI) method based on the particle-flux conservation law in Eq. (41). The present FPI method generalizes the earlier one by Park and Nägele[22] to shear-rate-dependent transport properties and cake formation. In the extended mBLA method, the axial pressure profile $P(z)$ needs to be determined numerically from solving Eq. (27). The physical quantities $\{z,\phi_w,R_c(z),v_w(z),u(y,z)\}$ are non-dimensionalized (reduced) here by their respective characteristic values $\{L,\phi_b,R_P^0,v_w^0,u^0\}$. For notational simplicity, unchanged symbols are used for the reduced quantities. The functional dependency of a quantity on the searched-for axial profiles $\phi_w(z)$ and $R_c(z)$ is indicated in its argument list by the standard bracket notation $[\phi_w]$ and $[R_c]$, respectively.

By splitting $\phi=(\phi-\phi_b)+\phi_b$ into its excess and bulk parts, respectively, the conservation law in Eq. (41) for the cross-sectionally averaged axial flux is rewritten as

$$\phi_b\langle u\rangle_R+\langle(\phi-\phi_b)u\rangle_R=\frac{\phi_b\,u^0}{2}, \tag{A1}$$

where $\langle\cdots\rangle_R=(1/\pi R^2)\int_S dS$ denotes the average over the cross-sectional area $S=\pi R^2$.

Substitution of the (formal) matched asymptotic solutions for ϕ and u into Eq. (A1) leads to the implicit integral equation in z,

$$\phi_w(z)=F(z,[\phi_w],[R_c])\equiv 1+\frac{\mathscr{B}(0,[\phi_w],[R_c])-\mathscr{B}(z,[\phi_w],[R_c])}{\mathscr{A}(z,[\phi_w],[R_c])}, \tag{A2}$$

where the functional dependencies on the concentration and cake resistance profiles are indicated explicitly. The dimensionless expressions for $\mathscr{A}$ and $\mathscr{B}$ are

$$\mathscr{A}(z,[\phi_w],[R_c])=\left\langle e^{-Pe_R\,v_w(z,[\phi_w],[R_c])}u(y,z,[\phi_w],[R_c])\right\rangle_R, \tag{A3}$$

$$\mathscr{B}(z,[\phi_w],[R_c])=\left\langle\left(1-Pe_R v_w(z,[\phi_w],[R_c])e^{-Pe_R v_w(z,[\phi_w],[R_c])}\right)\times u(y,z,[\phi_w],[R_c])\right\rangle_R, \tag{A4}$$

and these depend functionally on the searched-for concentration and resistance profiles.

In our numerical calculations, the (reduced) radial and axial coordinates are discretized uniformly in logarithmic space as $\log y_i=i\,\Delta\log y$ and equidistantly as $z_k=k\,\Delta z$, with step sizes $\Delta\log y$ and Δz, respectively, and integer indices i and k enumerating each grid point. In this way, the functional arguments of the axial profiles are approximated by arrays of N_z entries, namely, $[\phi_w^{(n)}]=[\phi_w^{(n)}(z_0),\phi_w^{(n)}(z_1),\ldots,\phi_w^{(n)}(z_{N_z})]$ and $[R_c^{(N)}]=[R_c^{(n)}(z_0),R_c^{(n)}(z_1),\ldots,R_c^{(n)}(z_{N_z})]$. The pressure profile, $P(z)$, determined by the differential equation in Eq. (27) is obtained numerically using a second-order finite difference method invoking a central difference scheme and a fictitious node method. The inlet pressure $P(0)$ is determined by the given value for the outlet pressure $P^L=P(L)=1$ atm and by the velocity, u^0, of the Hagen–Poiseuille feed flow at the inlet center. The numerically determined $P(z)$ is used for characterizing the axial dependencies of the flow profiles $v_w(z)$ and $u_z(z)=-(R^2/(4\eta_s))dP(z)/dz$.

On identifying F as the FPI integral operator, the iteration scheme,

$$\phi_w^{(n)}(z_k)=F(z_k,[\phi_w^{(n-1)}],[R_c^{(n-1)}]) \tag{A5}$$

is used for each axial position z_k, relating the concentration array $[\phi_w^{(n)}]$ at the n-th iteration step to the arrays $[\phi_w^{(n-1)}]$ and $[R_c^{(n-1)}]$ of the previous step $n-1$.

According to the thin cake model employed in this paper, no cake is formed at z_k when $\phi_w^{(n)}(z_k)<\phi_f$, and the corresponding hydraulic cake resistance value is set equal to zero, i.e., $R_c^{(n)}(z_k)=0$. If, instead, $\phi_w^{(n)}(z_{k^*})>\phi_f$ is found at some z_{k^*}, then $\phi_w^{(n)}(z_{k^*})$ is reset to $\phi_w^{(n)}(z_{k^*})=\phi_f$ and a suitable $R_c^{(n)}(z_{k^*})$ value is determined obeying the identity,

$$\phi_f=F(z_{k^*},[\phi_w^{(n-1)}],[R_c^{(n)}]). \tag{A6}$$

For this purpose, $[R_c^{(n)}]$ in the above-mentioned identity is taken to be equal to $[R_c^{(n-1)}]$, except for its k^*-th component treated as a free variable, determined from the requirement that the identity must be fulfilled. Note that Eqs. (A5) and (A6) are two conditions for the searched-for concentration and resistance profiles.

Once the arrays $[\phi_w^{(n)}]$ and $[R_c^{(n)}]$ of the discretized profiles are determined in the n-th iteration step, the under relaxed fixed-point iteration (FPI) scheme is applied individually to the arrays $[\phi_w^{(n)}]$ and $[R_c^{(n)}]$, according to

$$[\phi_w^{(n)}]=(1-\omega)[\phi_w^{(n)}]+\omega[\phi_w^{(n)}], \tag{A7}$$

$$[R_c^{(n)}]=(1-\omega)[R_c^{(n)}]+\omega[R_c^{(n)}], \tag{A8}$$

with an appropriately selected relaxation parameter $0<\omega<1$. The optimal choice of ω depends, in principle, on the operating conditions and dispersion properties. For the parameter sets C1 and C2

discussed in the present paper, $\omega = 0.01$ was found to be a good choice in most cases.

In the iteration procedure described above, the coupled flow and concentration fields are updated based on results from the previous iteration. At the initial zeroth-order step ($n = 0$), the concentration field is set equal to the uniform starting field $\phi^{(0)}(y,z) = \phi_b$ [which implies $R_c^{(0)}(z) = 0$]. The zeroth-order axial and radial flow fields, $u^{(0)}$ and $v^{(0)}$, and the zeroth-order pressure profile, $P^{(0)}$, are then computed numerically using $D_{yy}^{(0)} = D_{yy}(\phi, Pe_a = 0)$ and $\eta^{(0)} = \eta(\phi^{(0)}, \tilde{\tau} = 0)$ at each discretized grid point (y_i, z_k).

In the subsequent iteration steps ($n > 0$), the flow and concentration fields are updated as follows: First, the arrays $[\phi_w^{(n)}]$ and $[R_c^{(n)}]$ of the n-th iteration step are determined using the FPI method described above. Next, $P^{(n)}(z_k)$, $u^{(n)}(y_k, z_k)$ and $v^{(n)}(y_k, z_k)$ are numerically determined at the grid points (y_k, z_k). Using the updated (discretized) flow and concentration fields, the local shear rate and stress fields $Pe_a^{(n)}$ and $\tilde{\tau}^{(n)}$ are obtained. These are then used, in turn, to determine the viscosity field, $\eta^{(n)}$, and the radial diffusion coefficient field, $D_{yy}^{(n)}$, at all grid points (y_i, z_k). The iteration continues until both arrays, $[\phi_w^{(n)}]$ and $[R_c^{(n)}]$, have converged according to a prescribed criterion. For the employed high-precision criterion, about 3000 iteration steps were required to reach convergence when the cake was formed.

APPENDIX B: SIMPLIFIED mBLA PERMEATE FLUX EXPRESSION

On basis of the cross-sectionally averaged axial particle-flux conservation law in Eq. (41) and the asymptotically matched mBLA solutions for $u(y,z)$ and $\phi(y,z)$, we derive here a simplified expression for the length-averaged permeate flux, quoted in Eq. (43). Following earlier studies,[22,24] the axial particle flux, $J_z = \phi u$, is split into excess and bulk parts according to $J_z = J_z^{ex} + J_z^b$, where the bulk part is $J_z^b = \phi_b u$, such that J_z^{ex} vanishes outside the CP layer. Using this splitting, the conservation law in Eq. (41) reads [cf. also Eq. (A1)]

$$\langle J_z^{ex}\rangle_R = \frac{\phi_b u^0}{2} - \phi_b \langle u\rangle_R, \tag{B1}$$

where $\langle\cdots\rangle_R$ denotes the cross-sectional average. Next, using that $\langle u\rangle_R \approx \langle u^{out}\rangle_R$, where u^{out} is the axial velocity in the outer region given in Eq. (25), one obtains

$$\langle J_z^{ex}\rangle_R(z) = \frac{\phi_b u^0}{2}\left[1 - \frac{u(y=R,z)}{u^0}\right] = \frac{\phi_b u^0}{2}\beta^0 \frac{1}{L}\int_0^z \frac{v_w(z')}{v_w^0}dz'. \tag{B2}$$

Here, $\beta^0 = 4Lv_w^0/(Ru^0)$ is the characteristic solvent recovery indicator value introduced before in the context of Eq. (29). To obtain the second equality in Eq. (B2), volume conservation of solvent and particles expressed by $\nabla \cdot \mathbf{V} = 0$ was used. Volume conservation was likewise invoked for obtaining the pressure profile in Eq. (27).

An alternative expression for the cross-sectionally averaged excess flux is obtained from substituting the matched asymptotic mBLA expressions for u and ϕ into $J_z^{ex} = (\phi - \phi_b)u$ and subsequently performing the cross-sectional average by neglecting a term linear in ϕ_b. This leads to

$$\langle J_z^{ex}\rangle_R(z) \approx \frac{2\phi_w(z)u_z(z)}{R}\int_0^R dy\left[(1-y/R)(2-y/R)\mathscr{I}_\eta(y,z) \times \exp\left(-Pe_R\frac{v_w(z)}{v_w^0}\mathscr{I}_D(y,z)\right)\right], \tag{B3}$$

where the integrals $\mathscr{I}_\eta$ and $\mathscr{I}_D$ are given in Eqs. (39) and (40), respectively. From equating Eqs. (B2) and (B3), one obtains

$$\frac{\phi_b u^0}{2}\beta^0\frac{1}{L}\int_0^z \frac{v_w(z')}{v_w^0}dz' = 2\phi_w(z)u_z(z)\frac{1}{R}\int_0^R \psi(y,z)dy, \tag{B4}$$

where $u_z(z) = -(R^2/(4\eta_s))dP(z)/dz$ is the z-dependent factor of $u(y,z)$ in Eq. (25). The non-dimensional integrand,

$$\psi(y,z) = \left(1-\frac{y}{R}\right)\left(2-\frac{y}{R}\right)\mathscr{I}_\eta(y,z)\exp\left(-Pe_R\frac{v_w(z)}{v_w^0}\mathscr{I}_D(y,z)\right), \tag{B5}$$

related to $(\phi - \phi_b)u$, accounts for the intermingled effects of dispersion viscosity, radial diffusion coefficient, and osmotic pressure, the latter mediated via $v_w(z)$ in the Darcy–Starling boundary condition.

We next introduce simplifications for the radial integral of $\psi(y,z)$ appearing in Eq. (B4). On assuming $\eta = \eta_s$ and $D_{yy} = D_0$, and neglecting the osmotic pressure, which is justifiable in the UF to MF transition regime, one obtains $\mathscr{I}_\eta = \mathscr{I}_D = y/R$ and

$$\frac{1}{R}\int_0^R \psi(y,z)dy = \frac{6 - 6\,A(z) + 2\,A(z)^2 + (A(z)^2 - 6)\,e^{-A(z)}}{A(z)^4}, \tag{B6}$$

where

$$A(z) = Pe_R\frac{v_w(z)}{v_w^0}. \tag{B7}$$

Since $A(z) \gg 1$ holds within the mBLA description of crossflow, it suffices to account for the quadratic term in $A(z)$. The radial integral further simplifies to

$$\frac{1}{R}\int_0^R \psi(y,z)dy \approx \frac{2}{(Pe_R v_w(z)/v_w^0)^2}. \tag{B8}$$

This finding motivates us to define a dimensionless function $\Psi(z)$ by

$$\Psi(z) = \frac{(Pe_R v_w(z)/v_w^0)^2}{2}\frac{1}{R}\int_0^R \psi(y,z)dy, \tag{B9}$$

which is approximately equal to one for constant transport properties and zero osmotic pressure. When the particle transport is slowed down due to enlarged viscosity and reduced radial diffusion, values $\Psi(z) < 1$ are expected. In the opposite case, $\Psi(z)$ can be larger than one.

With this definition of Ψ inserted into Eq. (B4), we obtain

$$Pe_R^2 = \frac{8}{\beta^0}\frac{\phi_w(z)}{\phi_b}\frac{\Psi(z)}{\frac{u^0}{u_z(z)}\left(\frac{v_w(z)}{v_w^0}\right)^2\frac{1}{L}\int_0^z v_w(z')/v_w^0 dz'}. \tag{B10}$$

On noting that the radial characteristic Péclet number, $Pe_R = Rv_w^0/D_0$, is related to the axial characteristic Péclet number, $Pe_L = R^2u^0/(D_0L)$, by $\beta^0 = 4Pe_R/Pe_L$, the above-mentioned equation can be rewritten as

$$\left(Pe_R\frac{\langle v_w\rangle_L}{v_w^0}\right)^3 = 2Pe_L\frac{\phi_w(z)}{\phi_b}\frac{\Psi(z)}{G(z)}, \tag{B11}$$

where we have introduced the dimensionless function $G(z)$, defined as

$$G(z) = \frac{u^0}{u_z(z)}\frac{v_w^2(z)\frac{1}{L}\int_0^z v_w(z')dz'}{\langle v_w\rangle_L^3}, \tag{B12}$$

which is of order one at the outlet $z = L$. Equation (B11) is used as the starting point for Eq. (43) in Sec. IV. A decent approximation of $G(z)$ according to Eq. (B12) follows from replacing $v_w(z)$ and $u_z(z)$ by the mBLA forms for pure solvent (PS) feed, $v_w^{(PS)}(z)$ and $u_z^{(PS)}(z)$, without dispersion particles. The analytic expressions for the pure solvent flow profiles are given in the work by Park and Nägele[22] and thus are not repeated here.

REFERENCES

[1] E. A. Mason and H. K. Lonsdale, "Statistical-mechanical theory of membrane transport," J. Membr. Sci. **51**, 1–81 (1990).
[2] R. W. Baker, *Membrane Technology and Applications* (John Wiley & Sons, 2004).
[3] M. Mulder, *Basic Principles of Membrane Technology* (Springer, Netherlands, 2013).
[4] G. A. Truskey, F. Yuan, and D. F. Katz, *Transport Phenomena in Biological Systems* (Prentice Hall, 2009), p. 860.
[5] W. F. Blatt, A. Dravid, A. S. Michaels, and L. Nelsen, "Solute polarization and cake formation in membrane ultrafiltration: Causes, consequences, and control techniques," in *Membrane Science and Technology* (Springer, Boston, MA, 1970), pp. 47–97.
[6] M. C. Porter, "Concentration polarization with membrane ultrafiltration," Ind. Eng. Chem. Prod. Res. Dev. **11**, 234–248 (1972).
[7] D. R. Trettin and M. R. Doshi, "Limiting flux in ultrafiltration of macromolecular solutions," Chem. Eng. Commun. **4**, 507–522 (1980).
[8] G. Belfort, R. H. Davis, and A. L. Zydney, "The behavior of suspensions and macromolecular solutions in crossflow microfiltration," J. Membr. Sci. **96**, 1–58 (1994).
[9] R. K. Shah and A. L. London, *Laminar Flow Forced Convection in Ducts* (Academic Press, 1978), p. 492.
[10] G. Green and G. Belfort, "Fouling of ultrafiltration membranes: Lateral migration and the particle trajectory model," Desalination **35**, 129 (1980).
[11] P. Bacchin, P. Aimar, and R. W. Field, "Critical and sustainable fluxes: Theory, experiments and applications," J. Membr. Sci. **281**, 42–69 (2006).
[12] G. Belfort, "Membrane filtration with liquids: A global approach with prior successes, new developments and unresolved challenges," Angew. Chem., Int. Ed. **58**, 1892–1902 (2019).
[13] R. G. M. van der Sman and H. M. Vollebregt, "Transient critical flux due to coupling of fouling mechanisms during crossflow microfiltration of beer," J. Membr. Sci. **435**, 21–37 (2013).
[14] C. Y. Tang, T. H. Chong, and A. G. Fane, "Colloidal interactions and fouling of NF and RO membranes: A review," Adv. Colloid Interface Sci. **164**, 126–143 (2011).
[15] P. Bacchin, A. Marty, P. Duru, M. Meireles, and P. Aimar, "Colloidal surface interactions and membrane fouling: Investigations at pore scale," Adv. Colloid Interface Sci. **164**, 2–11 (2011).
[16] R. H. Davis and D. T. Leighton, "Shear-induced transport of a particle layer along a porous wall," Chem. Eng. Sci. **42**, 275–281 (1987).
[17] C. A. Romero and R. H. Davis, "Global model of crossflow microfiltration based on hydrodynamic particle diffusion," J. Membr. Sci. **39**, 157–185 (1988).
[18] R. H. Davis and J. D. Sherwood, "A similarity solution for steady-state crossflow microfiltration," Chem. Eng. Sci. **45**, 3203–3209 (1990).
[19] R. Roa, E. K. Zholkovskiy, and G. Nägele, "Ultrafiltration modeling of non-ionic microgels," Soft Matter **11**, 4106–4122 (2015).
[20] C. Pozrikidis, "Stokes flow through a permeable tube," Arch. Appl. Mech. **80**, 323–333 (2010).
[21] N. Tilton, D. Martinand, E. Serre, and R. M. Lueptow, "Incorporating Darcy's law for pure solvent flow through porous tubes: Asymptotic solution and numerical simulations," AIChE J. **58**, 2030–2044 (2012).
[22] G. W. Park and G. Nägele, "Modeling cross-flow ultrafiltration of permeable particle dispersions," J. Chem. Phys. **153**, 204110 (2020).
[23] G. A. Denisov, "Theory of concentration polarization in cross-flow ultrafiltration: Gel-layer model and osmotic-pressure model," J. Membr. Sci. **91**, 173–187 (1994).
[24] G. W. Park and G. Nägele, "Geometrical influence on particle transport in cross-flow ultrafiltration: Cylindrical and flat sheet membranes," Membranes **11**, 960 (2021).
[25] Y. A. Buyevich and S. K. Kapbsov, "Segregation of a fine suspension in channel flow," J. Non-Newtonian Fluid Mech. **86**, 157 (1999).
[26] M. Frank, D. Anderson, E. R. Weeks, and J. F. Morris, "Particle migration in pressure-driven flow of a Brownian suspension," J. Fluid Mech. **493**, 363–378 (2003).
[27] E. Nazockdast and J. F. Morris, "Microstructural theory and the rheology of concentrated colloidal suspensions," J. Fluid Mech. **713**, 420–452 (2012).
[28] J. F. Morris, "Toward a fluid mechanics of suspensions," Phys. Rev. Fluids **5**, 110519 (2020).
[29] H. Jin, K. Kang, K. H. Ahn, and J. K. G. Dhont, "Flow instability due to coupling of shear-gradients with concentration: Non-uniform flow of (hard-sphere) glasses," Soft Matter **10**, 9470–9485 (2014).
[30] J. Riest, T. Eckert, W. Richtering, and G. Nägele, "Dynamics of suspensions of hydrodynamically structured particles: Analytic theory and applications to experiments," Soft Matter **11**, 2821–2843 (2015).
[31] G. Nägele, J. K. G. Dhont, and T. Voigtmann, "Theory of colloidal suspension structure, dynamics, and rheology," in *Theory and Applications of Colloidal Suspension Rheology* (Cambridge University Press, 2021), pp. 44–119.
[32] A. S. Kim and Y. Liu, "Critical flux of hard sphere suspensions in crossflow filtration: Hydrodynamic force bias Monte Carlo simulations," J. Membr. Sci. **323**, 67–76 (2008).
[33] A. S. Kim and Y. Liu, "Irreversible chemical potential and shear-induced diffusion in crossflow filtration," Ind. Eng. Chem. Res. **47**, 5611–5614 (2008).
[34] C. G. de Kruif, E. M. F. van Iersel, A. Vrij, and W. B. Russel, "Hard sphere colloidal dispersions: Viscosity as a function of shear rate and volume fraction," J. Chem. Phys. **83**, 4717–4725 (1985).
[35] J. Mewis and N. J. Wagner, *Colloidal Suspension Rheology* (Cambridge University Press, 2012).
[36] H. Jin, K. Kang, K. H. Ahn, W. J. Briels, and J. K. G. Dhont, "Non-local stresses in highly non-uniformly flowing suspensions: The shear-curvature viscosity," J. Chem. Phys. **149**, 014903 (2018).
[37] G. Nägele, "On the dynamics and structure of charge-stabilized suspensions," Phys. Rep. **272**, 215 (1996).
[38] E. Guyon, J.-P. Hulin, L. Petit, and C. D. Mitescu, *Physical Hydrodynamics*, 2nd ed. (Oxford University Press, 2015).
[39] R. G. M. van der Sman, "Flow through a filter plate backed by a packed bed of spheres," Chem. Eng. Sci. **158**, 154–163 (2017).
[40] R. J. Hill, D. L. Koch, and A. J. C. Ladd, "Moderate-Reynolds-number flows in ordered and random arrays of spheres," J. Fluid Mech. **448**, 243–278 (2001).
[41] A. A. Zick and G. M. Homsy, "Stokes flow through periodic arrays of spheres," J. Fluid Mech. **115**, 13–26 (1982).
[42] I. M. Krieger, "Rheology of monodisperse latices," Adv. Colloid Interface Sci. **3**, 111–136 (1972).

[43]R. Roa, D. Menne, J. Riest, P. Buzatu, E. K. Zholkovskiy, J. K. G. Dhont, M. Wessling, and G. Nägele, "Ultrafiltration of charge-stabilized dispersions at low salinity," Soft Matter **12**, 4638–4653 (2016).
[44]A. J. Banchio, G. Nägele, and J. Bergenholtz, "Viscoelasticity and generalized Stokes–Einstein relations of colloidal dispersions," J. Chem. Phys. **111**, 8721–8740 (1999).
[45]M. Van Dyke, "Slow variations in continuum mechanics," Adv. Appl. Mech. **25**, 1–45 (1987).
[46]B. Marcos, C. Moresoli, J. Skorepova, and B. Vaughan, "CFD modeling of a transient hollow fiber ultrafiltration system for protein concentration," J. Membr. Sci. **337**, 136–144 (2009).
[47]P. Bacchin, D. Si-Hassen, V. Starov, M. J. Clifton, and P. Aimar, "A unifying model for concentration polarization, gel-layer formation and particle deposition in cross-flow membrane filtration of colloidal suspensions," Chem. Eng. Sci. **57**, 77–91 (2002).
[48]V. Aguirre-Montesdeoca, A. E. M. Janssen, A. Van der Padt, and R. M. Boom, "Modelling ultrafiltration performance by integrating local (critical) fluxes along the membrane length," J. Membr. Sci. **578**, 111–125 (2019).
[49]L. Song, "Why is the film model fundamentally wrong but still able to correlate the experimental data in membrane processes?," J. Membr. Sci. **686**, 121987 (2023).
[50]H. M. Vollebregt, R. G. M. van der Sman, and R. M. Boom, "Model for particle migration in bidisperse suspensions by use of effective temperature," Faraday Discuss. **158**, 89–103 (2012).
[51]D. Y. Kwon, S. Vigneswaran, A. G. Fane, and R. Ben Aim, "Experimental determination of critical flux in cross-flow microfiltration," Sep. Purif. Technol. **19**, 169–181 (2000).
[52]V. L. Vilker, C. K. Colton, and K. A. Smith, "The osmotic pressure of concentrated protein solutions: Effect of concentration and pH in saline solutions of bovine serum albumin," J. Colloid Interface Sci. **79**, 548–566 (1981).
[53]H. M. Vollebregt, R. G. M. van der Sman, and R. M. Boom, "Suspension flow modelling in particle migration and microfiltration," Soft Matter **6**, 6052–6064 (2010).
[54]E. C. Eckstein, D. G. Bailey, and A. H. Shapiro, "Self-diffusion of particles in shear flow of a suspension," J. Fluid Mech. **79**, 191 (1977).